R-1303

HEL PHASE CONTROL

by

Kenneth W. Kaiser

September 1979

The Charles Stark Draper Laboratory, Inc.

Cambridge, Massachusetts 02139

U4169

Accession Number: 4169

Publication Date: Sep 01, 1979

Title: HEL Phase Control

Personal Author: Kaiser, K.W.

Corporate Author Or Publisher: Charles Stark Draper Laboratory Inc., 555 Technology Square, Cambridge Report Number: R-1303

Report Prepared for: U.S. Army Missile Research and Development Command, Redstone Arsenal, AL 35809 Report Number Assigned by Contract Monitor: SLL 80 1019

Comments on Document: Archive, RRI, DEW

Descriptors, Keywords: HEL High Energy Laser Closed Loop Phase Control Thermal Blooming Deformable Mirror Compensation Control Continuous Wave Pulse

Pages: 00092

Cataloged Date: Dec 11, 1992

Contract Number: DAAK40-78-C-0117

Document Type: HC

Number of Copies In Library: 000001

Record ID: 25818

Source of Document: DEW

REPORT DOCUMENTATION PAGE		READ INSTRUCTIONS BEFORE COMPLETING FORM
1. REPORT NUMBER	2. GOVT ACCESSION NO.	3. RECIPIENT'S CATALOG NUMBER
4. TITLE *(and Subtitle)* HEL PHASE CONTROL		5. TYPE OF REPORT & PERIOD COVERED Technical Report
		6. PERFORMING ORG. REPORT NUMBER R-1303
7. AUTHOR*(s)* Kenneth W. Kaiser		8. CONTRACT OR GRANT NUMBER*(s)* DAAK40-78-C-0117
9. PERFORMING ORGANIZATION NAME AND ADDRESS The Charles Stark Draper Laboratory, Inc. 555 Technology Square Cambridge, Massachusetts 02139		10. PROGRAM ELEMENT, PROJECT, TASK AREA & WORK UNIT NUMBERS
11. CONTROLLING OFFICE NAME AND ADDRESS U.S. Army Missile R&D Command Redstone Arsenal, Alabama 35809		12. REPORT DATE September 1979
		13. NUMBER OF PAGES 92
14. MONITORING AGENCY NAME & ADDRESS *(if different from Controlling Office)*		15. SECURITY CLASS. *(of this report)* Unclassified
		15a. DECLASSIFICATION/DOWNGRADING SCHEDULE

16. DISTRIBUTION STATEMENT *(of this Report)*

Approved for public release; distribution unlimited.

17. DISTRIBUTION STATEMENT *(of the abstract entered in Block 20, if different from Report)*

18. SUPPLEMENTARY NOTES

19. KEY WORDS *(Continue on reverse side if necessary and identify by block number)*

High-Energy Laser (HEL)
Closed-Loop Phase Control
Thermal Blooming
Deformable Mirror

20. ABSTRACT *(Continue on reverse side if necessary and identify by block number)*

This report summarizes progress toward a solution to the problem of HEL control-loop instability in the presence of thermal blooming. Current phase-control-loop structure is analyzed, and a dual-loop structure is proposed. A corresponding closed-loop phase-compensation control algorithm is also proposed, and its fundamental requirements identified. Because the key subsystem impacted by the control algorithm is the HEL deformable mirror, considerable attention is paid to adaptive-optics deformable-mirror requirements for both continuous-wave and pulsed lasers.

7512F376

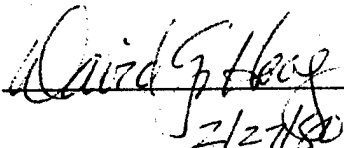DD FORM 1473 EDITION OF 1 NOV 65 IS OBSOLETE
1 JAN 73

R-1303

HEL PHASE CONTROL

by

Kenneth W. Kaiser

September 1979

Approved: _____

The Charles Stark Draper Laboratory, Inc.
Cambridge, Massachusetts   02139

ACKNOWLEDGMENT

TABLE OF CONTENTS

SECTION 1

INTRODUCTION

The assumed objective of a high-energy-laser (HEL) beam-control system is to deliver maximum fluence to the target, despite laser, atmospheric, and target disturbances. As shown in Figure 1, the laser and atmosphere introduce significant phase distortions into the beam, whereas the unknown and variable reflectivity of the target introduces amplitude disturbances in the delivered energy.
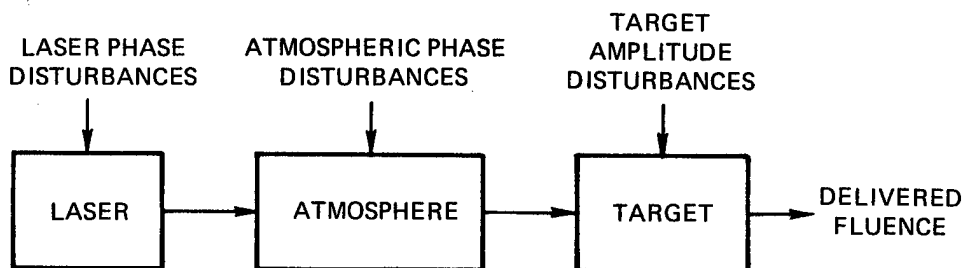
Figure 1. HEL beam-propagation model.

The Army HEL scenario and HEL capabilities impose several constraints on the solution to this problem. Clearly, if a direct measurement of delivered fluence were available, then the design of a closed-loop controller for maximal fluence delivery would be a straightforward matter; but the scenario rules out amplitude measurement. In addition, amplitude modification of the beam is not within the capability of the laser at the present time. Consequently, HEL beam control must be performed solely with beam phase measurements and phase modification.

1

The use of closed-loop phase control systems to enhance laser performance is not new. Several systems have been proposed in the past and demonstrated at low power in the laboratory. But simulations at higher power levels, such as those required for the HEL, have clearly indicated a lack of desired performance: the control loop becomes unstable in the presence of atmospheric disturbances, particularly in the presence of moderate to heavy thermal blooming.

This report is directed toward a solution to this problem. In Section 2, phase-control-loop structure is analyzed, and a dual-loop structure is proposed as an effective means of compensating for the multiple disturbances encountered at high power levels. A corresponding closed-loop phase-compensation control algorithm is proposed, and its fundamental requirements identified.

The structure of the proposed control algorithm is based on the observation that phase-conjugate compensation of thermal blooming is not stable in the HEL application. Thus, the algorithm is designed to use phase-conjugate correction of the total measured phase error, with an additional correction for the focus error caused by thermal blooming. Consequently, the phase-sensing process requires not only a wavefront sensor, but the ability to extract the blooming focus component. Considerable attention is devoted to this problem in Section 3.

The approach to the development of the control algorithm is to present an extensive physical model, which is based on an algebraic beam-propagation model.[1]* The modeling effort proceeds in two steps. First, because it is simple, a model of the static control loop and the associated thermal-blooming physics is developed. This appears in Section 4. In Section 5, the model is generalized to the more complex dynamic case. It is noted that these models may also be used to set HEL phase-control subsystem requirements and component specifications, or may be of value in quantitative system trade studies.

_____

* Superscript numerals refer to similarly numbered items in the List of References.

The key subsystem that will be impacted by the control algorithm is the deformable mirror used for phase compensation. The report refers to remedies for the severe deformable-mirror performance limitations that presently exist in the continuous-wave case, and Section 6 presents a study of mirror actuator requirements for the pulsed-laser case.

SECTION 2

PHASE-CONTROLLER STRUCTURE AND
CONTROL ALGORITHM FOR
ATMOSPHERIC-DISTURBANCE COMPENSATION

2.1   Controller Structure

This section examines the impact of control theory on the HEL
beam-control problem.   Section 2.1.1 presents an example which illustrates
that the best controller structure for handling atmospheric disturbances
at high power levels, i.e., one which can control at least two disturb-
ances, requires two control loops.   The conclusions developed in presenting
this example are applied to the HEL beam-control problem in Section 2.1.2.

2.1.1   Structure Required for Multiple Disturbances

The philosophy basic to designing the structure of closed-loop
controllers for multiple disturbances is that a disturbance should not
be propagated around the control loop any further than is necessary.
The reason is that the further a disturbance propagates, the worse the
initial null acquisition transient, and the higher the rms error is
near null.

The impact of controller structure on null performance is illus-
trated with a simple example.   A two-disturbance process with two simple
dynamic lags (τ) is shown in Figure 2.   It is assumed that x and y are
random white-noise disturbances, and that the variable z is to be held
near a null value of zero by a proportional feedback controller with a
gain, K.   The best structure for this controller is found by comparing
two alternatives: single loop or dual loop.

4
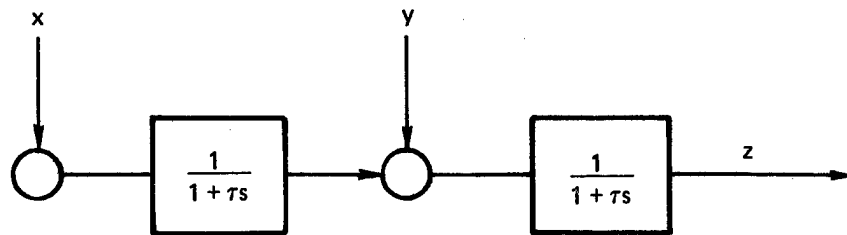
Figure 2. Two-disturbance process.

The single proportional loop structure is shown in Figure 3. Note that the disturbance x must propagate all the way to the output z before it is sensed by the controller. Also, the disturbance y must propagate through the first dynamic block before it is controlled. This situation results in relatively poor control of the variable z.
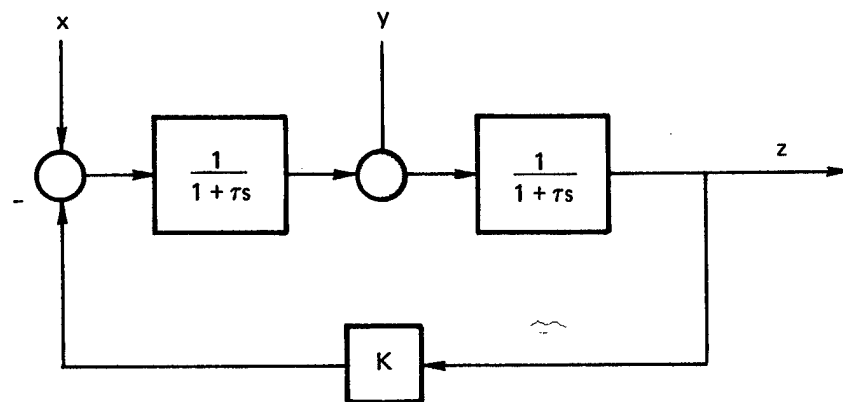
Figure 3. Single-loop structure.

The Laplace transform domain expression for z obtained from Figure 3 is

$$z(s) = h_1(s)y(s) + h_2(s)x(s)$$

5

where

$$h_1(s) = \frac{(1 + \tau s)}{(\tau^2 s^2 + 2\tau s + 1 + K)}$$

$$h_2(s) = \frac{1}{(\tau^2 s^2 + 2\tau s + 1 + K)}$$

It is assumed that x and y are random uncorrelated white-noise disturbances, with variances σ_x^2 and σ_y^2.

In this case, the expression for the variance at the output σ_z^2 is given by[2]

$$\sigma_z^2 = \frac{1}{2\pi j} \int_{-j\infty}^{+j\infty} \left(h_1(s)h_1(-s)\sigma_y^2 + h_2(s)h_2(-s)\sigma_x^2\right) ds$$

Evaluation of this variance for h_1 and h_2 results in

$$\sigma_z^2 = \left[\frac{1}{4\tau} + \frac{1}{4\tau(K+1)}\right]\sigma_y^2 + \left[\frac{1}{4\tau(K+1)}\right]\sigma_x^2$$

To reduce the output variance as much as possible, the value of controller gain, K, should be large. The resulting large-gain variance for the single-loop controller is

$$\sigma_z^2 = \frac{1}{4\tau}\sigma_y^2 + \frac{1}{4\tau K}\sigma_x^2 \tag{1}$$

Note that little control over the disturbance y is available from this single-loop controller configuration.

6

The alternative to the single-loop controller is shown in Figure 4. A dual-loop structure allows control of the disturbance x
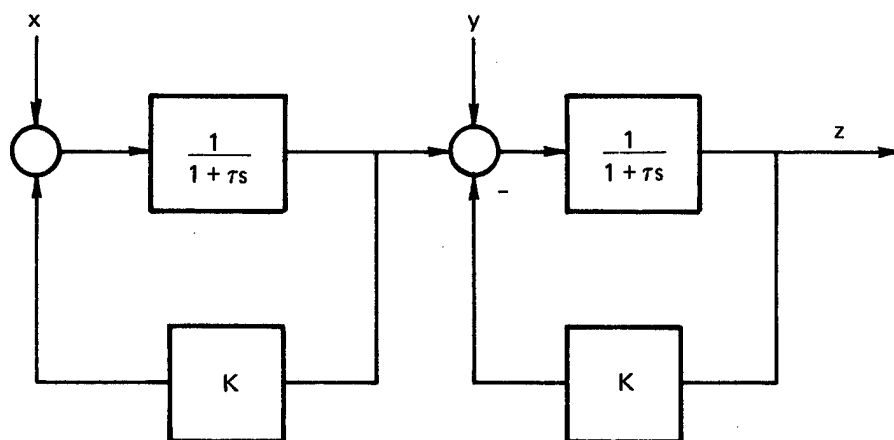
Figure 4. Dual-loop structure.

before it propagates to the output z. Also, the disturbance y is controlled without propagating through an additional dynamic block. The dual-loop structure results in the following values of h_1 and h_2

$$h_1(s) = \frac{1}{(\tau s + K + 1)}$$

$$h_2(s) = \frac{1}{\tau^2 s^2 + 2\tau s (K + 1) + (K + 1)^2}$$

Evaluation of the variance integral in this case results in

$$\sigma_z^2 = \left[\frac{1}{2\tau (K + 1)}\right]\sigma_y^2 + \left[\frac{1}{4\tau (K + 1)^3}\right]\sigma_x^2$$

As in the single-loop case, the best controller gain for reducing the variance of the output z is a large value of K. The resulting large gain variance for the dual-loop controller is

$$\sigma_z^2 = \frac{1}{2\tau K} \sigma_y^2 + \frac{1}{4\tau K^3} \sigma_x^2 \qquad (2)$$

A comparison of the large gain-variance expressions, Eq. (1) and (2), indicates that a significant reduction in the rms error of the output variable is possible with the dual-loop configuration, but not with the single-loop configuration. For example let

$$\tau = 1 \text{ second}$$

$$K = 10^6$$

$$\sigma_x = \sigma_y = 1 \text{ watt/Hz}$$

The values for the resulting variance of z are

$$\text{Single loop:} \quad \sigma_z^2 = 2.5 \times 10^{-1}$$

$$\text{Dual loop:} \quad \sigma_z^2 = 5.000 \times 10^{-7}$$

The dual-loop configuration thus reduces the null variance by a factor of 2×10^{-6}.

Clearly, the control-loop structure has a significant influence on reducing the rms error of the controlled output. Consequently, it is an important consideration in HEL beam control.

2.1.2 Proposed Structure for HEL Beam Control

The single-loop configuration shown in Figure 5 is the control
structure that has been used in laboratory beam-control experiments.
It is commonly referred to as a Coherent Optical Adaptive Techniques
(COAT) loop. The advantage of this single-loop structure is that it
requires only one phase-disturbance sensor. It is noted, however, that
low-power lasers have clean beams and only one source of disturbances.

```
        DISTURBANCE          DISTURBANCE
             |                    |
             v                    v
      +-------------+      +-------------+      +-------------+
   -->|    LASER    |----->| ATMOSPHERE  |----->|   TARGET    |-------->
  |   +-------------+      +-------------+      +-------------+      |
  |                                                                 |
  |   +-------------+      +-------------+      +-------------+      |
  |   |   PHASE     |<-----|  CONTROL    |<-----|   PHASE     |<-----
   ---|  CORRECTOR  |      | ALGORITHM   |      | MEASUREMENT |
      +-------------+      +-------------+      +-------------+
```
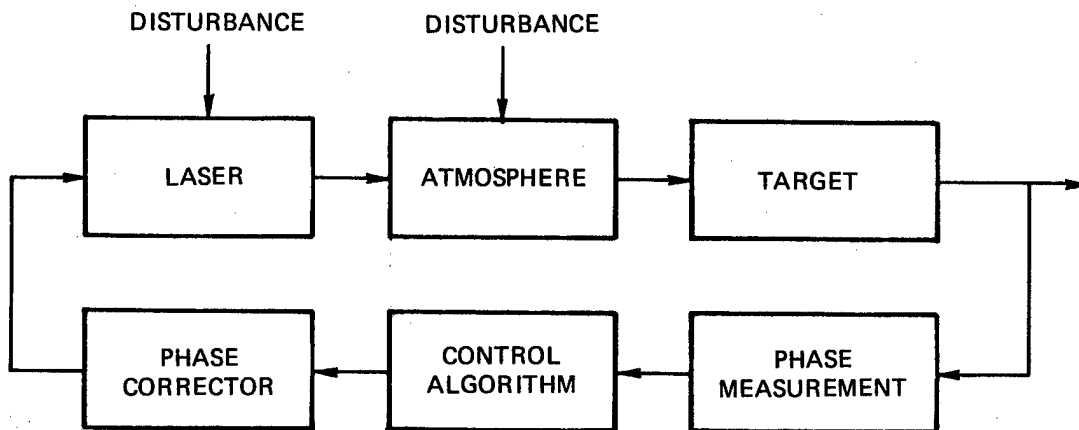
Figure 5. Single control loop (COAT loop).

The single-loop structure has disadvantages which make it parti-
cularly unsuitable for high-power multiple-disturbance HEL applications.
With the single-loop structure, laser-cavity aberrations must propagate
all the way to the target and back before correction. If phase correc-
tion is done in the laser cavity, e.g., via phase conjugators, then
atmospheric disturbances must be propagated into the laser cavity for
correction. This results in a difficult target-acquisition-transient
problem, and a higher rms error in the beam maintenance mode of opera-
tion, which means lower power on target. For large aberrations, the com-
pounding of the disturbances before correction could give rise to non-
linear effects which would further aggravate the phase-measurement problem.

9

The dual-loop configuration appearing in Figure 6 is similar to the configuration shown in Figure 4. Much tighter control over the disturbances is possible. The advantages of this controller structure are easier target acquisition and lower rms error in the beam maintenance mode of operation, which means higher power on target.

Because the dual-loop configuration shown in Figure 6 contains a hardware redundancy, the alternate configuration shown in Figure 7 is proposed for HEL beam control. By changing the location of the phase corrector, i.e., a deformable mirror, both laser-cavity aberrations and atmospheric-disturbance errors can be corrected, while the desirable features of the dual-loop structure are retained.

Both dual-loop structures (Figure 6 and Figure 7) have separate phase measurements for the laser and atmosphere loops. This is highly desirable due to the nonlinearity of the atmospheric correction (see Section 2.2).

2.2   Control Algorithm

Existing algorithms are inadequate for phase correction of atmospheric disturbances encountered at high power levels, and experience in the HEL community has determined that phase-conjugate compensation of thermal blooming is not stable. Again, it is pointed out that if an intensity measurement of the target return were available, then the blooming control algorithm would be simple, and no stability problems would be encountered. However, such an intensity measurement is ruled out by the Army scenario. Intensity gradients can be measured via multidither techniques, but more information is required for stabilization and control over a wide range of conditions. The image-sharpening algorithm is mathematically equivalent to phase-conjugate control, and does not properly address the correction of thermal blooming. However, image sharpening with a low-power mirror is a good method for obtaining a wide-band phase measurement from the target return. Consequently, it is assumed that such a phase measurement is available for data input to the control algorithm.
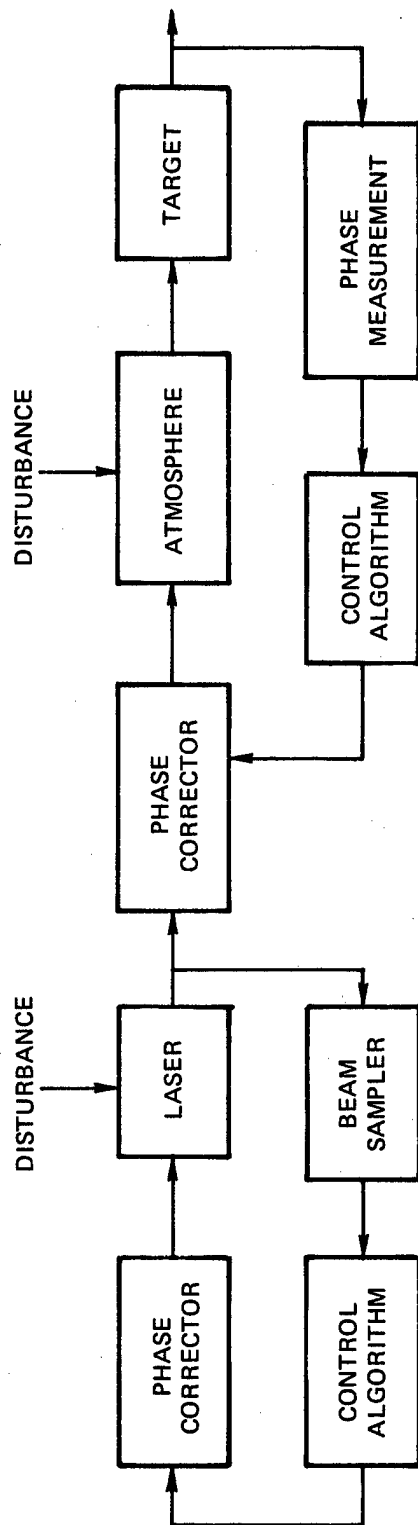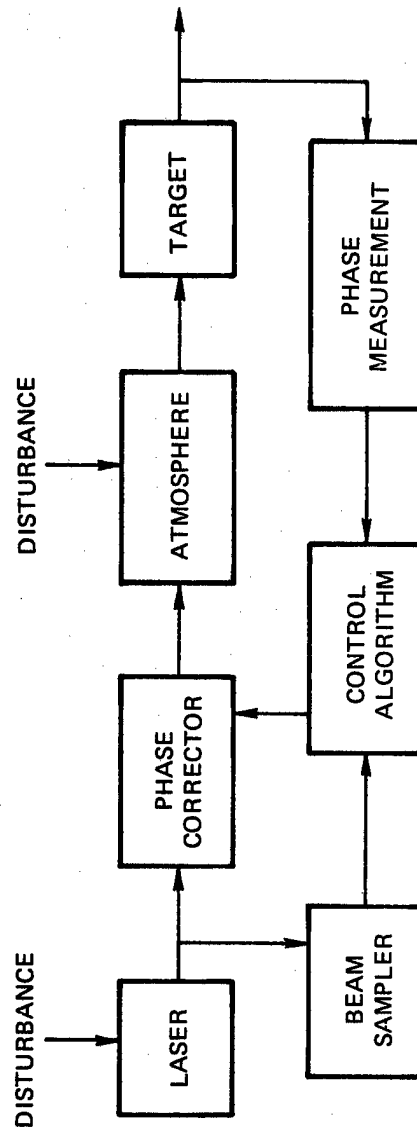
10

Figure 6. Dual-loop configuration.

Figure 7. Alternate dual-loop configuration.

11

There are indications that such a phase measurement can provide a basis for a successful algorithm. It is known that a phase correction forced at the aperture interacts with the atmosphere in a nonlinear manner, resulting in control-loop instability for phase-conjugate correction. The nature of the problem is a counterproductive response to excessive confinement of light rays, which indicates that the problem is dominated by the focus-error term caused by thermal blooming. This indicates that a focus-modified version of phase conjugation would be optimal.

The control algorithm proposed for HEL atmospheric-error correction has been developed assuming that:

(1)   Atmospheric disturbances consist of turbulence and thermal blooming.

(2)   The controller has the dual-loop structure shown in Figure 4.

(3)   The beam cleanup loop is working and is noninteractive with the atmospheric correction loop.

It is further assumed that the algorithm for turbulence effects consists of dynamic compensation and a phase-conjugate correction.

The thermal-blooming phase error is split into a focus error and the remaining blooming phase error. A dynamically compensated phase-conjugate correction is applied to all thermal-blooming phase errors except focus. The blooming focus error is controlled by application of a dynamically compensated optimal correction determined from the algebraic model. A diagram of this control algorithm appears in Figure 8.

An alternative algorithm structure would apply a phase-conjugate correction of the entire measured error, with an additional corrective term for the thermal-blooming focus error. A diagram of this algorithm configuration appears in Figure 9, where the term $K_B(F)$ is a nonlinear corrective term dependent on the amount of focus error, F.

12
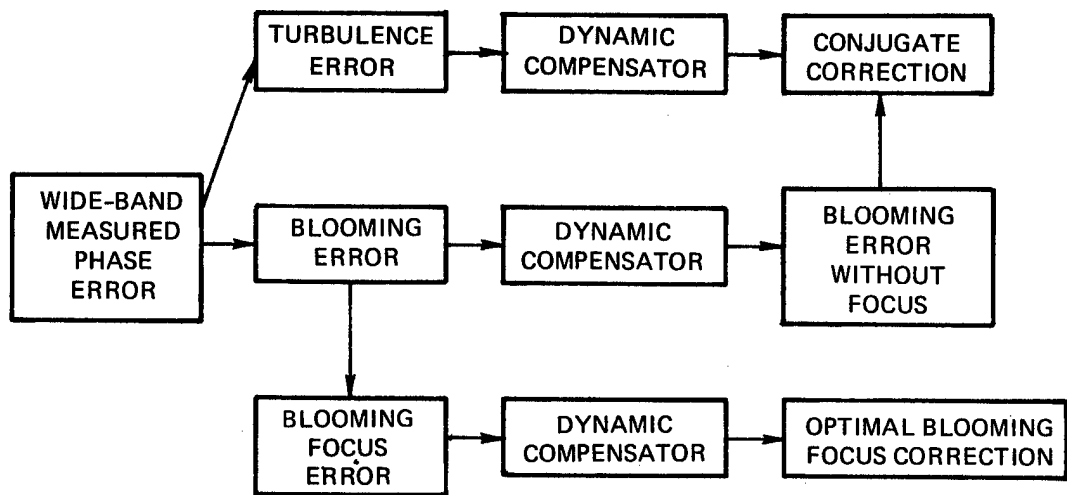
Figure 8.   Control algorithm structure.
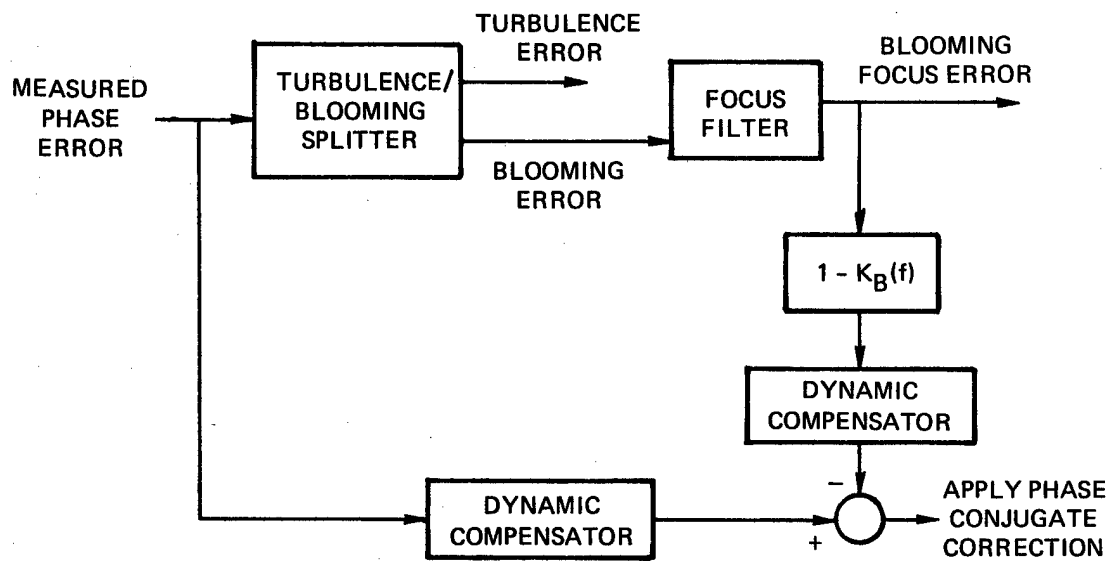
Figure 9.   Alternative control algorithm structure.

SECTION 3

ISOLATION OF THERMAL-BLOOMING EFFECTS

Because use of the control algorithm proposed in Section 2.2 depends on specific correction of the thermal-blooming focus error, this error must be separated from other atmospheric-disturbance errors. In turn, this requires that thermal-blooming effects be isolated from turbulence effects. Discrimination may be accomplished on the basis of the spatial and dynamic characteristics of beam phase distortions.

3.1   Consideration of Atmospheric-Disturbance Dynamics

3.1.1   Thermal Blooming

Since thermal blooming is a deterministic process, its characteristic dynamics[3] are obtained by examining the on-axis long-time blooming transient

$$\frac{I(0,z,t)}{I(0,0,0)} = \epsilon^{-\alpha z} \epsilon^{-t/\tau_L}$$

where $I(0,0,0)$ is the on-axis intensity at the aperture at $t = 0$, and $I(0,z,t)$ is the on-axis intensity at a range, z, and time, t. The thermal-blooming time constant is given by

$$\tau_L = \frac{\rho C_p N_0 a^2}{-2\mu_T \alpha I_0 z^2}$$

14

The various terms and representative numbers are

$$\frac{\rho C_p N_0}{-\mu_T} = 1290 \text{ joules/cm}^2$$

$$\alpha z = 0.1 \qquad \text{(attenuation)}$$

$$a = 0.5 \text{ m} \qquad \text{(beam radius)}$$

$$z = 1 \text{ km} \qquad \text{(range)}$$

$$I_0 = 127.3 \text{ W/cm}^2 \qquad (10^6 \text{ watts total power})$$

The resulting value of the thermal blooming time constant is

$$\tau_L = 1.18 \text{ seconds}$$

It is seen that thermal blooming is a low-pass process in the frequency domain with a transfer function of $1/(1 + \tau_L s)$. A typical frequency response plot of this process appears in Figure 10.
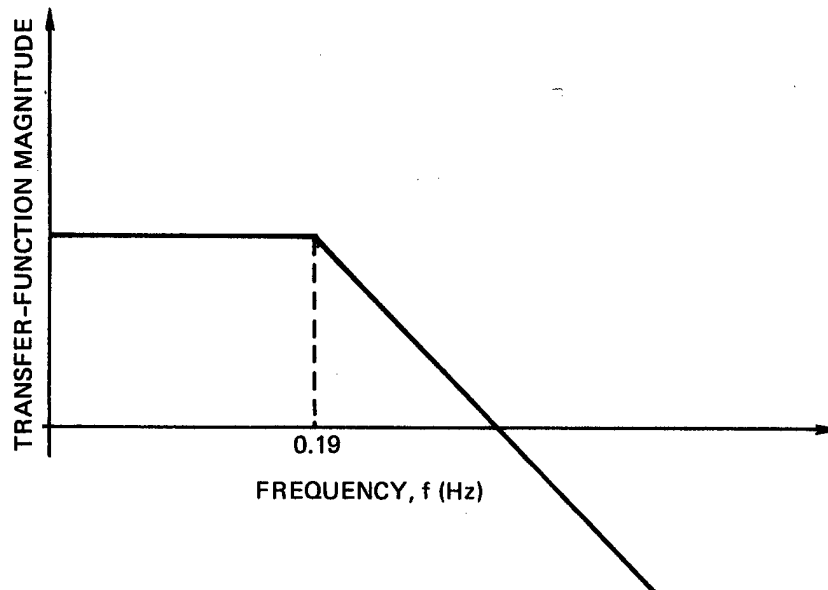
Figure 10. Thermal-blooming frequency response.

3.1.2 Turbulence

Since the temporal behavior of turbulence is a random process, its dynamic behavior is obtained from its power spectral density (PSD). Furthermore, since a turbulence/blooming splitter is followed by a focus filter, it is speculated that we need only examine the turbulence-focus PSD.

The random variable $C_3(t)$ is the component of focus due to turbulence. The turbulence-focus autocorrelation function is given by

$$R_{33}(\tau) = \overline{C_3(t)C_3(t + \tau)}$$

and the corresponding PSD is obtained from

$$S_{33}(\omega) = \int_{-\infty}^{+\infty} R_{33}(\tau)\varepsilon^{-j\omega\tau}\, d\tau$$

It is shown in Reference 4 that the PSD S_{33} has the form shown in Figure 11, with the low- and high-frequency cutoff points given by

$$f_L = \frac{0.05v}{R}$$

$$f_H = \frac{0.5v}{R}$$

where v is the transverse wind velocity, and R is the radius of the transmitter aperture.

For the case where R = 0.5 meter and v = 200 meters per second, it is found that $f_L = 20$ Hz and $f_H = 200$ Hz. This PSD is shown in Figure 12.

16
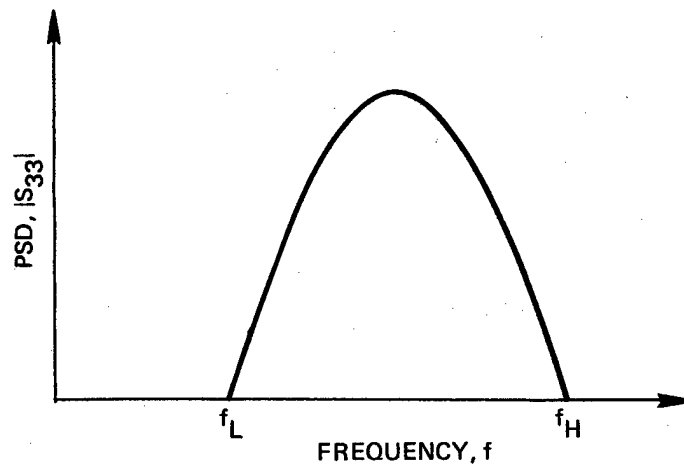
Figure 11. Turbulence-focus PSD.
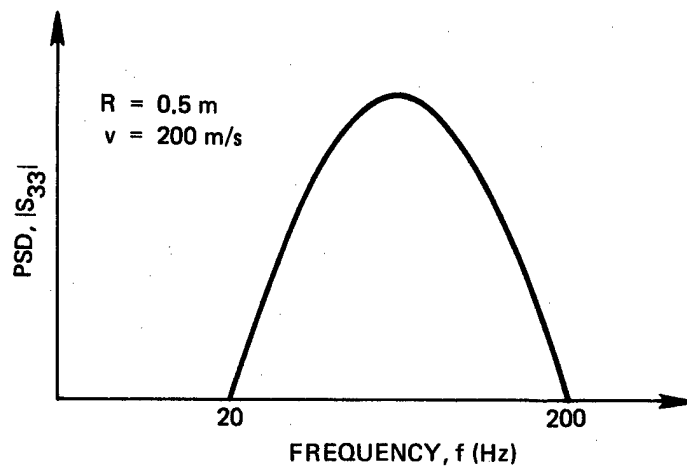
Figure 12. Turbulence-focus PSD.

17

3.2   Separation of Thermal-Blooming and Turbulence Effects

3.2.1 High-Frequency Turbulence/Blooming Splitter

It can be seen that the turbulence and thermal-blooming dynamic processes shown in Figure 10 and Figure 12 have disjoint spectra and can easily be separated with a simple low-pass/high-pass filter assembly when the turbulence focus PSD is in a high-frequency region. This is illustrated in Figure 13.
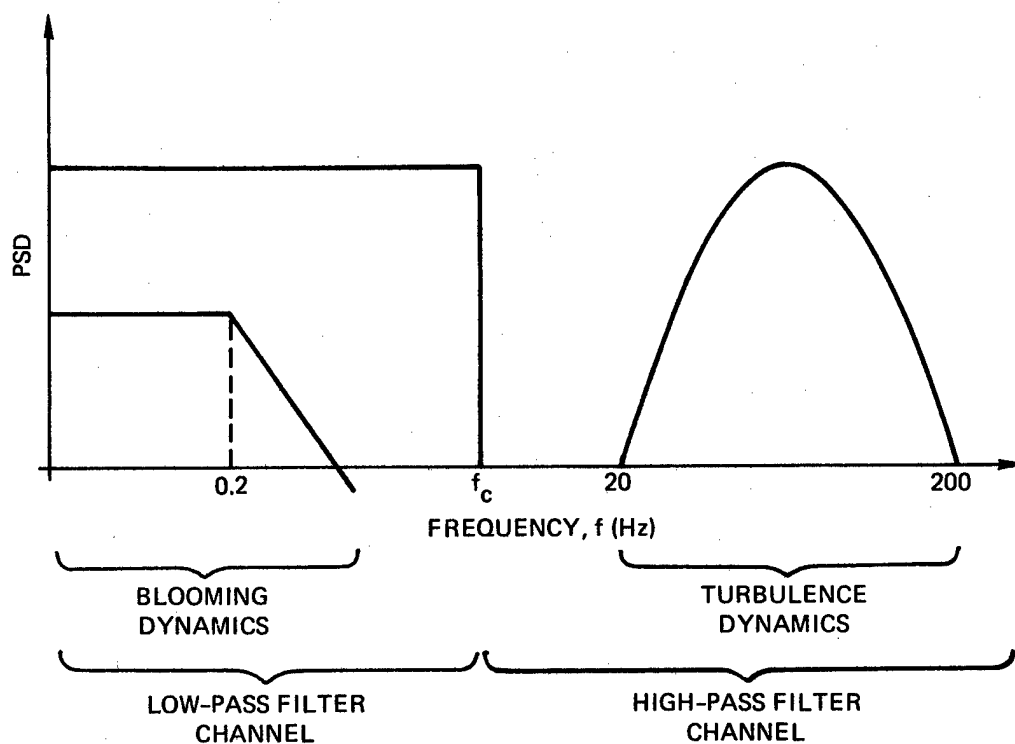
Figure 13. Turbulence/blooming splitter.

Two requirements for the low-pass/high-pass filter assembly are: simplicity and an easily adjustable crossover frequency, f_c. Simplicity is desired to keep the data-processing load down, and thereby minimize the delay time associated with the phase measurement. The easily

18

adjustable crossover frequency is a useful feature for adjusting opera-
tional hardware from test data and measurements. This feature also allows
for the possibility of changing the crossover frequency in an adaptive
manner under changing operating conditions.

It is possible to construct the high-pass/low-pass filter assembly
from a single low-pass filter. The reason for this is that a high-pass
filter is the complement of a low-pass filter. This high-pass/low-pass
interconnection is shown in Figure 14.
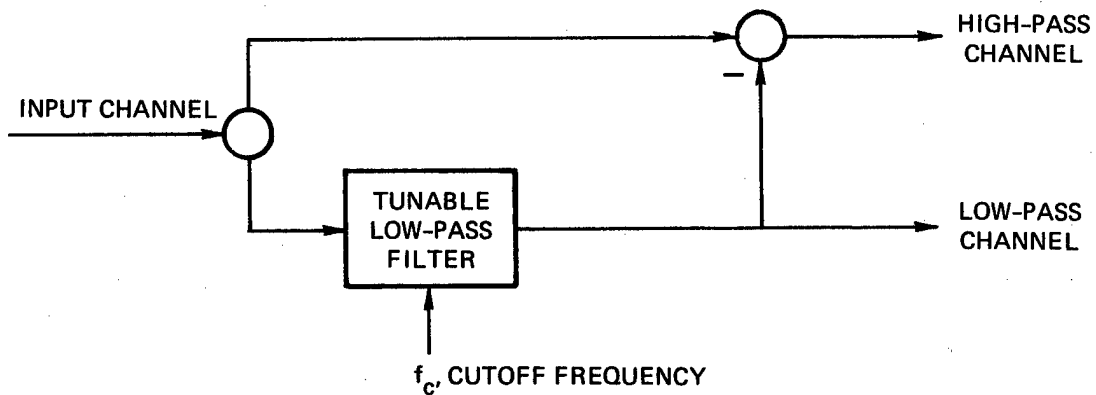
Figure 14. Low-pass/high-pass filter assembly.

Since the spectra of the two atmospheric-disturbance processes in
Figure 14 are disjoint, then the low-pass filter is not critically de-
pendent on the process models, which are only approximate. Consequently,
complex filters such as the Kalman filter need not be employed, and filter
simplicity can be obtained via classical filtering techniques. A Butter-
worth low-pass filter, for example, would be adequate.

Butterworth filters can be constructed of any dynamic order; how-
ever, experience has indicated that a third-order filter will satisfy
most computational needs. A third-order Butterworth filter has a transfer
function given by

$$\frac{\omega_c^3}{s^3 + 2\omega_c s^2 + 2\omega_c^2 s + \omega_c^3}$$

19

with a magnitude frequency function given by

$$\frac{1}{\sqrt{1 + \left(\dfrac{\omega}{\omega_c}\right)^6}}$$

where ω_c is the filter-cutoff frequency.

The magnitude of this filter's frequency response appears in Figure 15 and its transient response is shown in Figure 16. A block diagram of the digital form of this filter is shown in Figure 17 to illustrate the simplicity and easy online filter tuning capability.
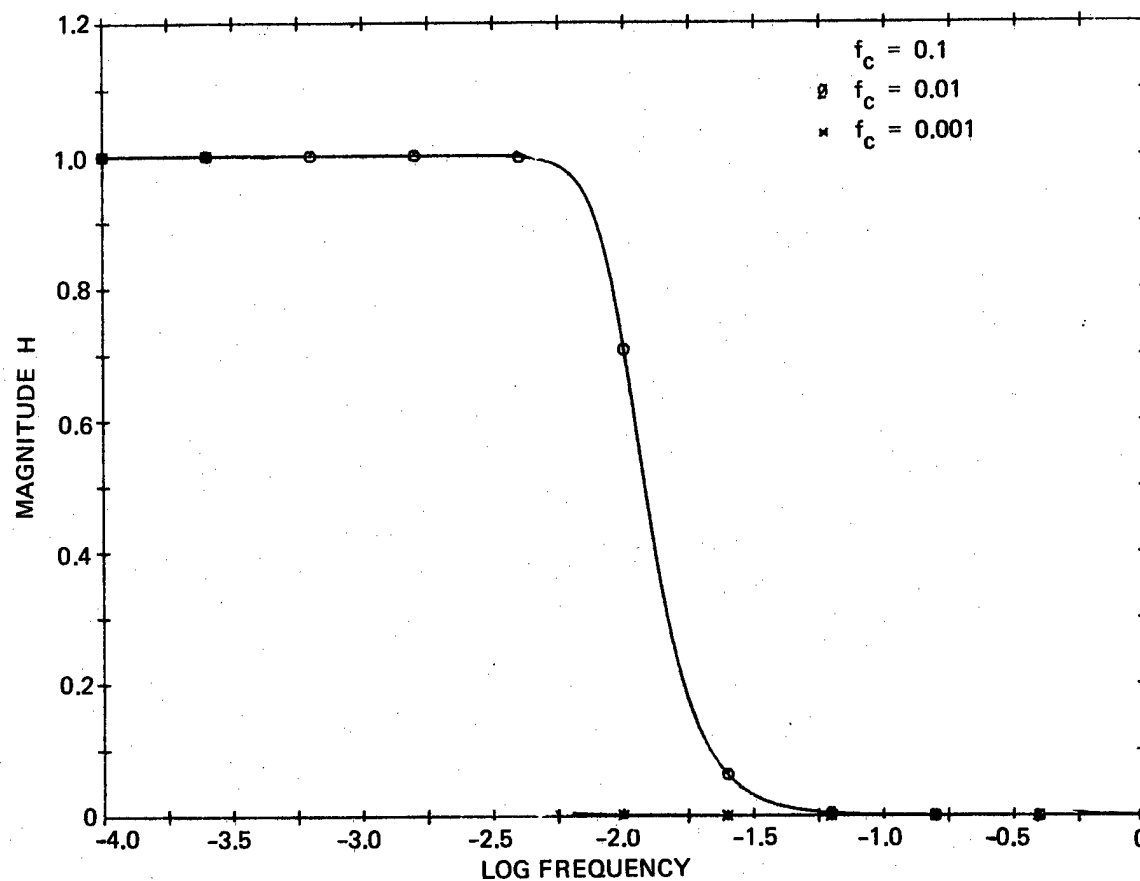
Figure 15. Butterworth filter frequency response.
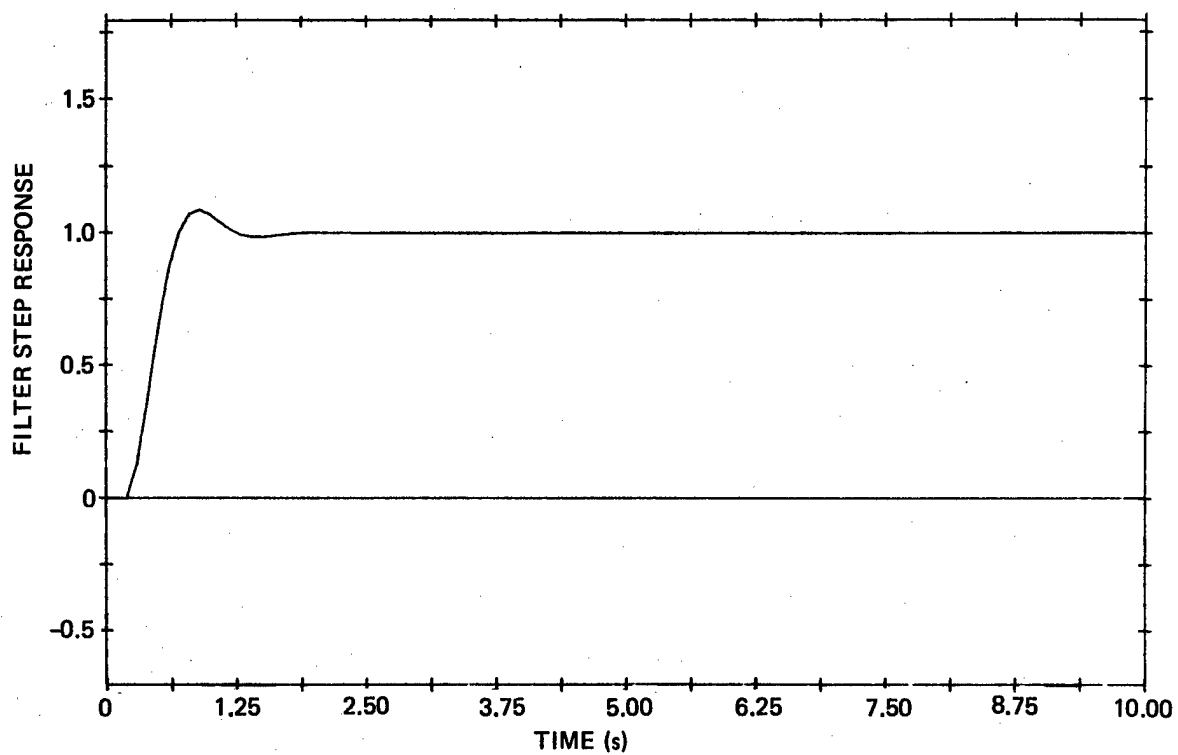
Figure 16.   Butterworth filter transient response.
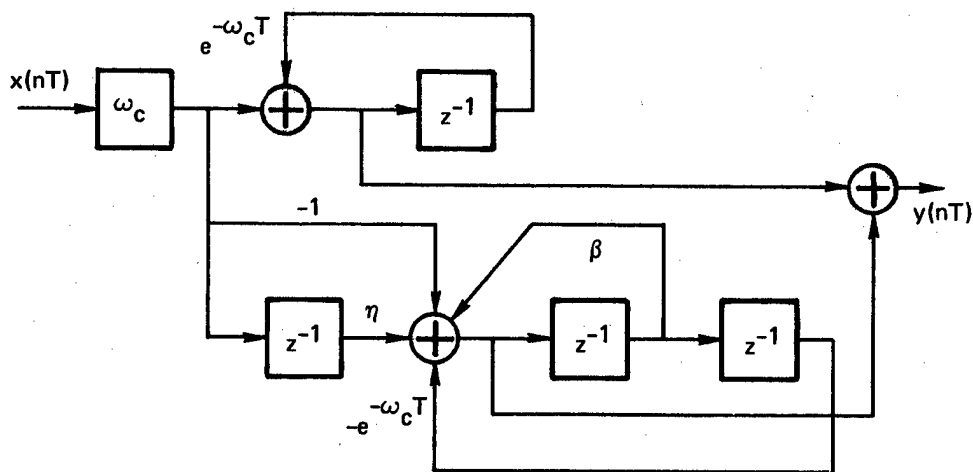
$$\beta = 2 \exp[-\omega_c T/2] \cos (\sqrt{3}\,\omega_c T/2)$$

$$\eta = \exp[-\omega_c T/2][\cos (\sqrt{3}\,\omega_c T/2) + (\sin (\sqrt{3}\,\omega_c T/2))/\sqrt{3}\,]$$

Figure 17.   Three-pole Butterworth low-pass digital filter.

3.2.2 Low-Frequency Turbulence/Blooming Splitter

The high-pass/low-pass filter assembly will not separate turbulence and blooming effects under all conditions. In particular, it cannot separate turbulence and blooming when the turbulence-focus PSD shifts downward in frequency with decreasing transverse wind velocity. This effect is illustrated in Figure 18. Consequently, there exists a lower bound on the transverse wind velocity, below which the turbulence and blooming cannot be easily distinguished on the basis of dynamic behavior. This limiting case is illustrated in Figure 19. A turbulence lower cut-off frequency of 1.19 Hz corresponds to a transverse wind velocity of 1.9 meters per second (4.25 miles per hour). The problem now arises as to how to separate the focus due to turbulence and blooming for low wind velocities and spectral overlap, as indicated in Figure 20.
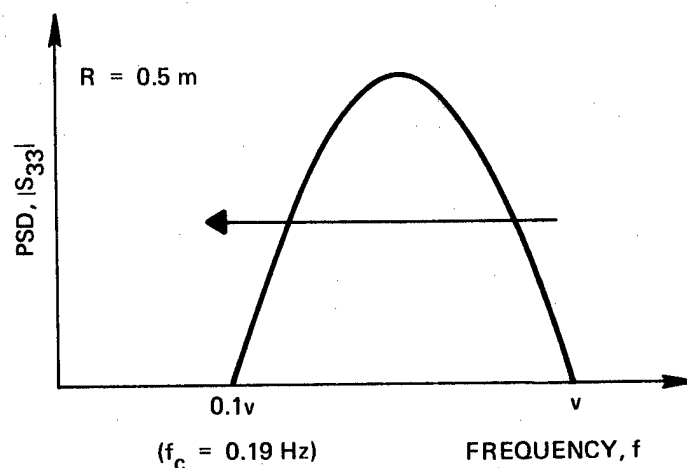
Figure 18. Turbulence PSD shift with wind velocity.

v_L = 1.9 m/s = 4.25 mi/h
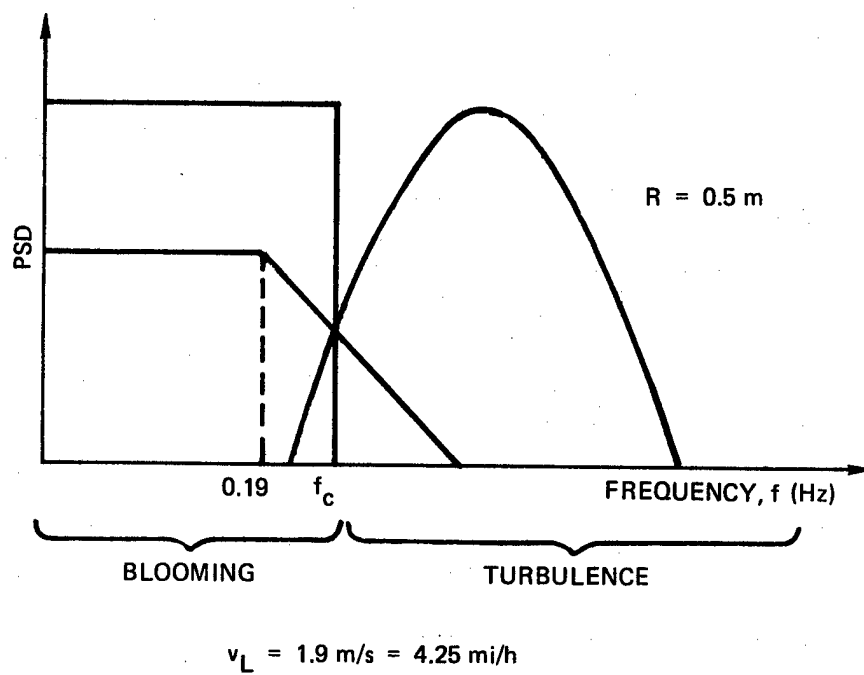
Figure 19. Lower limit on wind velocity for disjoint spectra.
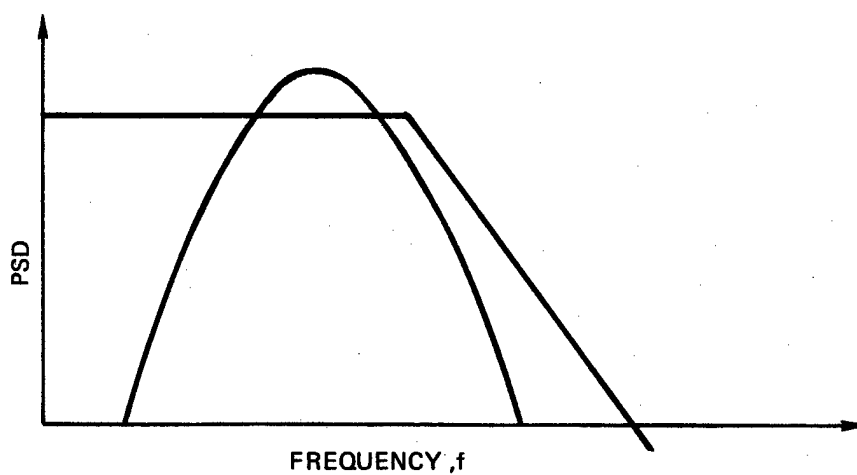
Figure 20. Low-wind spectral-overlap case.

23

Before seeking a solution to this problem, the relative magnitudes should be investigated. As shown in Figure 21, the magnitude of turbulence focus may be insignificant in the region of spectral overlap. If this is true, then the algorithm is simple: assume that all of the low-frequency focus is due to thermal blooming, and apply the optimal correction. According to Reference 4, it is quite possible that this could be the case.
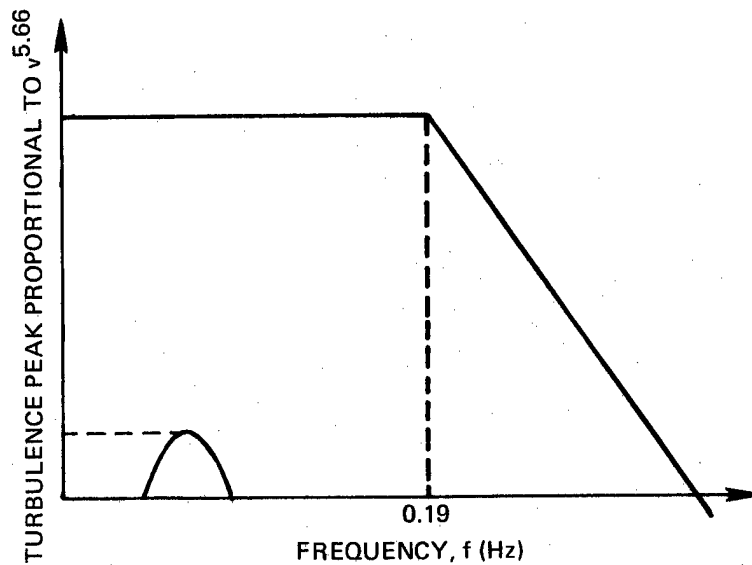
Figure 21. Magnitude of low-wind spectral overlap problem.

In order to see this, the total energy in the low-frequency turbulence focus is approximately computed. The total low-frequency energy, E, is given by

$$E_3 = \int_{f_L}^{f_H} S_{33}(f)\, df$$

24

and is approximately equal to

$$E_3 \approx \frac{1}{2}\left(f_H - f_L\right)S_p$$

where S_p is the peak value of turbulence focus. Using the expressions for f_H and f_L, and assuming that the peak value, S_p, is proportional to $v^{5.66}$, leads to

$$E_3 \approx \frac{Cv^{6.66}}{4R}$$

where C is a constant. Thus, for small values of v, the total energy due to focus turbulence is proportional to $v^{6.66}$ in the region of spectral overlap.

It is observed that the focus error due to thermal blooming is constant in this region, and does not diminish with v at all. Consequently, for small velocities, v, it is quite possible that the turbulence focus error could be small compared to the thermal-blooming focus error, and could be neglected. However, this possibility cannot be determined with current high-frequency nonzero-velocity models,[4] which are the only tools available at this time. This can be seen from the following analysis of the expressions developed in Reference 4 for turbulence focus PSD.

These expressions have the asymptotic form

$$S_{33}(f) \rightarrow \left(\frac{v}{fR}\right)^{11/3}$$

for f >> v/R. This model cannot be applied to the case of low frequency and zero velocity because of the following limiting situations.

For the situation where v approaches zero, we obtain the condition

$$S_{33}(f) \rightarrow 0$$

for f >> 0. Consequently, the low-frequency regime where f = 0 is not modeled by this expression. Where f → 0, we obtain

$$S_{33}(f) \rightarrow \infty$$

for 0 >> v/R. It is seen that this condition is not met even when v = 0.

The best path at this time seems to be to develop a low-frequency low-velocity turbulence-focus PSD model, and follow up with a reanalysis of the situation to see if further work on the turbulence/blooming splitter is required for the low-frequency low-velocity regime.

3.3   Focus Filter

In the event that turbulence and blooming must be separated when there is low wind spectral overlap, it must be accomplished by studying the blooming versus turbulence phase profile characteristics. That is, focus error alone cannot be determined to arise from either turbulence or blooming. However, the total blooming phase would have spatial peculiarities that would allow blooming and turbulence to be distinguished. Consequently, one would have to perform the turbulence/blooming splitting operation first, then apply the focus filter.

The design of a suitable focus filter is a straightforward operation, since only one spatial integral is involved. If $\Phi(x,y,t)$ is the input phase signal, $P_3(x,y)$ denotes the focus Zernike mode, and $C_3(t)$ is the output focus term, then they are related as follows

$$C_3(t) = \iint_{\text{aperture}} \Phi(x,y,t) P_3(x,y) \, dx \, dy$$

26

The C_3 operator is independent of time, and requires a spatially weighted sum of the phase sample points. If the input phase is sampled on a spatial grid continuously in time, then the focus filter can be hard wired with no time delay. If, however, the input phase is measured by a scanning technique, then a simple recursive computation is possible, and C_3 is available in time at the frame-scan rate.

SECTION 4

STATIC CONTROL MODEL: OPTIMAL
THERMAL-BLOOMING FOCUS-ERROR CORRECTION

Development of thermal-blooming focus-error correction requires a model of the thermal-blooming process suitable for closed-loop phase-controller design. This model, along with a suitable performance index, provides the basis for developing an optimal feedback control law. The purpose of considering a control model for the static (steady-state) case is to develop an optimal stable steady-state null controller. The static model has been developed, however, such that it can be generalized to the dynamic case, which is presented in Section 5.

A block diagram of the static control model appears in Figure 22. Each block of the diagram is explained in the following subsections.

4.1   Thermal-Blooming-Process Block

The static model of the thermal-blooming process was developed from the algebraic propagation model.[1] This model does not require new modeling effort, but is an application of the algebraic propagation model[1] to closed-loop controller design. The thermal-blooming-process model involves developing an expression for the thermal-blooming aberration as a function of the scenario parameters and the control aberration forced at the aperture.
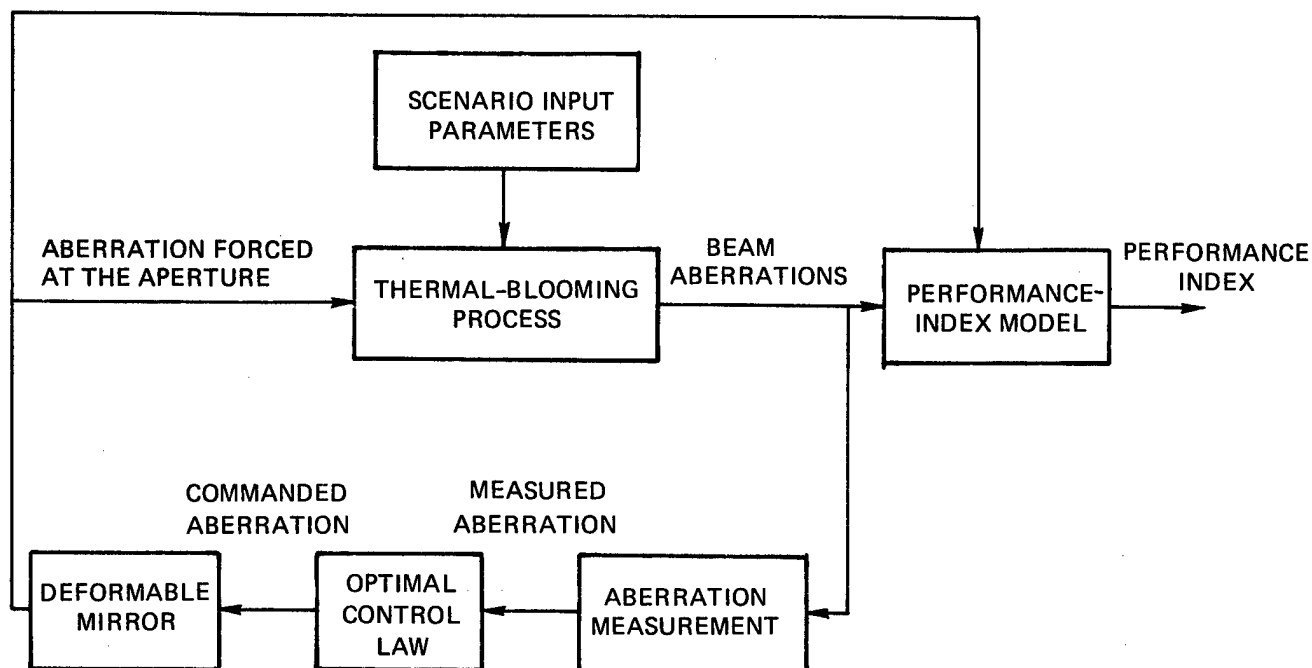
Figure 22. Static control model.

The variables involved are as follows. X is the normalized control aberration forced at the aperture

$$X = \frac{\sigma_{F3}}{\sigma_D}$$

and Y is normalized aberration from thermal blooming

$$Y = \frac{\sigma_B}{\sigma_D}$$

where σ_{F3} is the focus dispersion forced at the aperture, σ_B is the developed blooming dispersion, and σ_D is diffraction limit. The remaining terms are scenario parameters: (1)

(1) N_D: distortion number.

(2) N_F: Fresnel number.

(3) N_Q: laser quality number.

(4) T: transmission.

(5) D: parameter grouping.

(6) C_B': beam descriptor.

(7) a: beam descriptor.

The derivation of the expression for Y in terms of X and the scenario parameters is straightforward, but lengthy. Consequently, the details of this derivation appear in Appendix A. A diagram of the thermal-blooming process appears in Figure 23.

SCENARIO
INPUT
$[N_D, N_F, N_Q,$
$T, D, C_B', a]$

FORCED
ABERRATION

X

THERMAL-
BLOOMING
ABERRATION

$$\sqrt{C_B' (N_D\, N_F\, T)^a}\; (1+2X^2)^{\frac{2-a}{4}}\; \ell n^{\frac{a}{2}} \left| \frac{\left(\frac{2\,N_F}{D}\right)}{X + \sqrt{X^2 + \left(\frac{2\,N_Q}{N_F}\right)^2 \left(\frac{N_F}{D} - X\right)^2}} \right|$$

Y
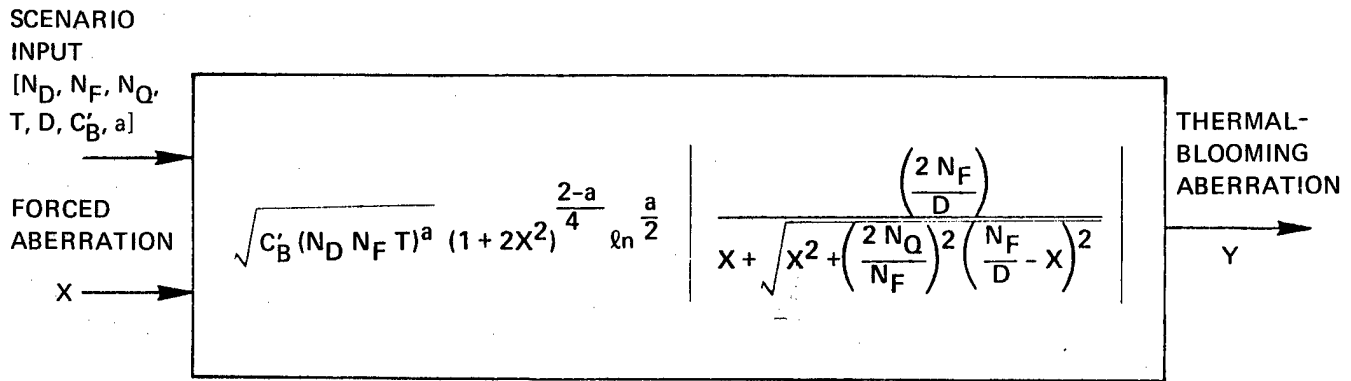
Figure 23. Model block for thermal blooming.

4.2 Aberration-Measurement Block

The static model of beam-aberration measurement consists of adding measurement noise. The mathematical model for static measurement is

$$Y_{measured} = Y_{actual} + Y_{noise}$$

30

where Y_{noise} is characterized by statistical properties such as the measurement noise, mean $\bar{Y}_{noise}$, and covariance, Σ_Y. A diagram for the aberration-measurement block appears in Figure 24.

$$Y_{NOISE}, \Sigma_Y, \bar{Y}_{NOISE}$$

$$Y_{ACTUAL} \longrightarrow \bigcirc \longrightarrow Y_{MEASURED}$$
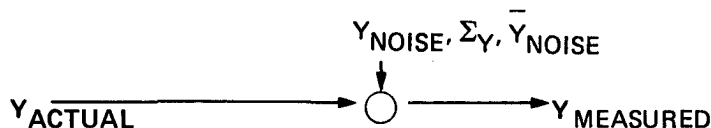
Figure 24. Block for aberration measurement.

4.3 Deformable-Mirror Block

The static model for the deformable mirror consists of a saturation function of the commanded aberration. That is

$$X_{FORCED} = SAT[X_{COMMAND}]$$

where

$$SAT(U) = \begin{cases} U \text{ if } |U| \leq A \\ A \text{ if } U > A \\ -A \text{ if } U < -A \end{cases}$$

A is the saturation threshold and U is an input variable. This function accounts for the fact that the deformable mirror cannot experience an unlimited amount of deflection. The diagram for this block appears in Figure 25.
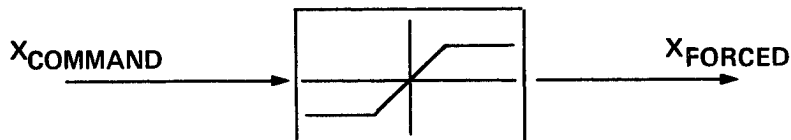
$$X_{COMMAND} \longrightarrow \boxed{\quad} \longrightarrow X_{FORCED}$$

Figure 25. Block for aberration forced at the aperture.

4.4   Optimal-Control-Law Block

The most general form for the optimal control law is a negatively fed back nonlinear function of the measured aberration.   That is

$$X_{COMMAND} = -F(Y_{measured})$$

where the nonlinearity $F(\cdot)$ is the control law for the special blooming focus correction.   The object of the analysis is to determine the form of this function $F(\cdot)$.   Other types of control laws are included in this model.   For example, if

$$F(Y) = Y$$

we have a phase conjugate controller which is linear negative feedback with a gain of 1.   A generalization of the phase conjugate controller is given by

$$F(Y) = KY$$

which is a linear negative feedback with a gain of K.

One approach to determining the special correction is to look for an optimal gain, K.   If such a value of K is dependent on the aberration, Y, then there is no such optimal constant gain, and the resulting control law is a nonlinear function of Y.   Experience has indicated that phase-conjugate control is not optimal.   Consequently, the general model of a nonlinear function is used in developing the optimal control.   The diagram for the optimal-control-law block appears in Figure 26.

Figure 26.   Block for optimal control law.

4.5   Performance-Index Model

The performance index for the beam-aberration control algorithm is the peak intensity on target. The optimal control law is chosen such that this index is maximized for all thermal-blooming corrective action applied by the controller. The performance-index model is developed as follows.

We start with the peak intensity on target given by the algebraic propagation model[1]

$$I_P = \frac{PT}{2\pi z_t^2 \sigma_x \sigma_y} \tag{3}$$

where P is power and z_t is the target range. The convention in modern control theory is to determine control laws that minimize some performance index, J. To adhere to this convention, Eq. (3) is inverted and normalized as follows

$$J_{total} = \frac{\pi z_t^2 \sigma_D^2}{PT} \left[\frac{2\sigma_x \sigma_y}{\sigma_D^2} \right]$$

where σ_D is the diffraction limit. Again, from the algebraic model, it is found that

$$2\sigma_x \sigma_y = \sigma_D^2 + 2\left(\sigma_{F3}^2 + 0.85\sqrt{2}\ \sigma_{F3}\sigma_B + 0.36\sigma_B^2 \right) \tag{4}$$

Straightforward derivation of Eq. (4) would normally result in two numerical changes: in place of $0.85\sqrt{2}$, one would obtain $\sqrt{\sqrt{2}}$, and in place of 0.36, one would obtain 0.5. However, correction of the modes higher than focus has been assumed, and taking this into account provides the result in Eq. (4). Use of this result provides

$$J_{total} = \frac{\pi z_t^2 \sigma_D^2}{PT} [1 + J_B]$$

where

$$J_B = 2(X^2 + 0.85\sqrt{2}\ XY + 0.36Y^2)$$

J_B is the thermal-blooming performance index. Minimization of J_B provides the maximum target intensity in the presence of thermal blooming. The performance index block appears in Figure 27.

FORCED ABERRATION

J_B

X
$$2(X^2 + 0.85\sqrt{2}\ XY + 0.36\ Y^2)$$

Y

PERFORMANCE
INDEX

**THERMAL-
BLOOMING
ABERRATION**
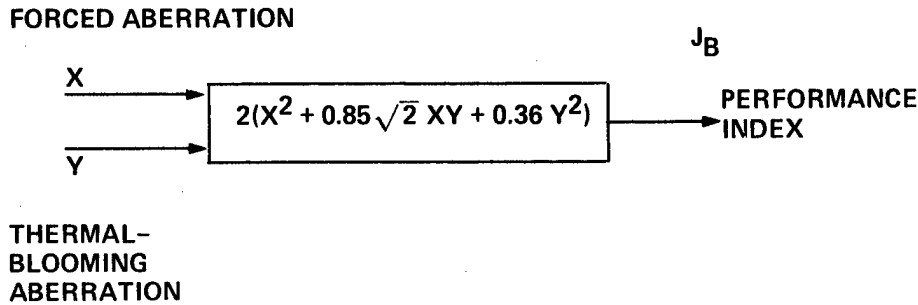
Figure 27. Performance-index-model block.

4.6 Uses of the Static Control Model

The static control model in Figure 28 shows detailed relationships between the scenario parameters, the control law, F(Y), and the performance index, J_B. Several uses for this model are apparent. The model provides a detailed basis for synthesizing an optimal control F(Y) such that J_B is minimized for all scenario inputs in a given parameter space. This static optimal control law constitutes the special correction for blooming-induced focus error, and is the primary motivation for development of the detailed model.

The model can also be used to generate system specifications. For example, the model allows one to determine the maximum allowable value of measurement noise covariance, Σ_Y, in terms of the performance index, J_B. This is an efficient means of generating measurement accuracy

34
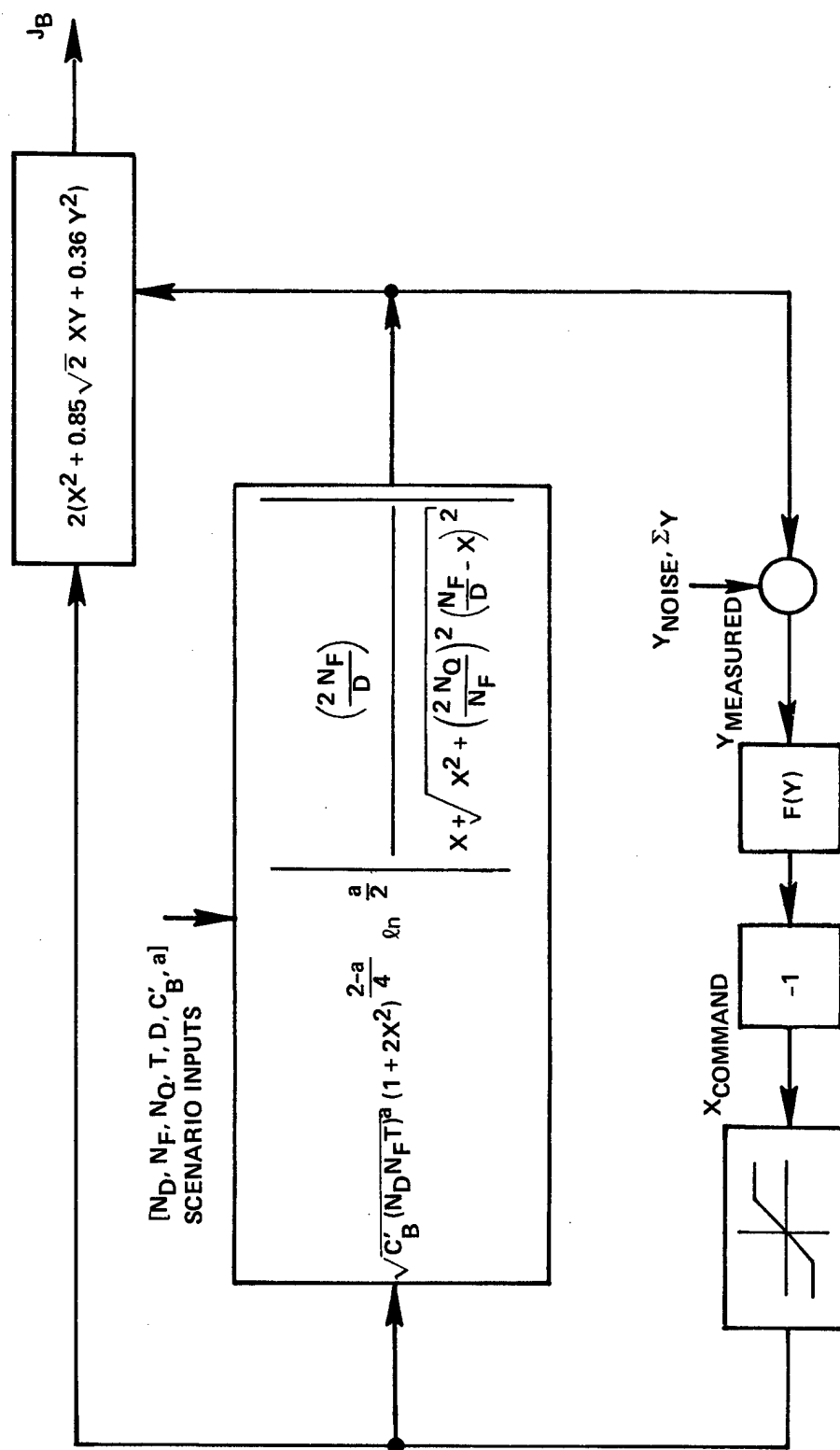
Figure 28. Static control model of thermal blooming.

requirements in terms of the peak intensity on target. If one allows too large a measurement error, then system performance degradation is excessive. On the other hand, if one has a measurement system that is more accurate than necessary, then the system will be unnecessarily costly for the unneeded accuracy.

Another use of the model is to generate a specification for the allowable saturation level of the deformable mirror in terms of J_B. This ensures that the mirror deformation capability would be set in a manner consistent with the parameter space of the system.

SECTION 5

DYNAMIC CONTROL MODEL:
OPTIMAL DYNAMIC COMPENSATION

The dynamic control model is developed by generalizing the static control-loop model presented in Section 4. The analysis supporting the design of the dynamic model addresses two primary issues: closed-loop stability and system transient response. Other issues, such as determining dynamic specifications for various system components are also investigated. This section presents the dynamic model for the optimal compensation design.

The dynamic model is based on the HEL algebraic propagation model.[1] Although the propagation model includes time-varying terms, it required extension for the dynamic model. Since this material is new to the HEL community, more emphasis on the details of the propagation model is provided in this section than was done for the static control model.

To properly account for dynamic effects, the following terms must be added to the terms used to describe the static model:

(1) Self-blooming parameter dynamics.

(2) Heating dynamics of beam.

(3) Measurement dynamics.

(4) Deformable-mirror dynamics.

(5) Feedback-controller dynamics for optimal dynamic compensation.

The self-blooming parameter already exists in the time-varying version of the algebraic propagation model, and is not a new effect. The remaining terms in the list are new and are developed on a block by block basis in the following sections.

The dynamic closed-loop thermal-blooming model appears in Figure 29. The block diagram follows the general structure outlined in Figure 22, except that the various functions are now distributed over several blocks. The structure of Figure 22 is used to explain the various parts of the model. All of the constants and variables are identified in Table 1, for ease of reference.

5.1 Thermal-Blooming-Process Block

The thermal-blooming process shown in Figure 22 is distributed over several blocks in Figure 29. In addition, due to the number of variables required by the model, normalization does not offer the advantage of simplification and has not been employed. The block labeled "algebraic propagation model" is essentially the same as the static thermal-blooming-process model shown in Figure 23.

The difference in the dynamic case is that this model becomes time varying through the self-blooming parameter, $m(t)$. The output of the algebraic propagation model is the developed phase, ψ_h. This phase is not a physically measurable variable, but instead is a driving function that gives rise to the actual phase, $\bar{\psi}_h$, through thermal-blooming dynamics. These variables—developed phase, ψ_h, and actual phase, $\bar{\psi}_h$—interact in a manner analogous to stress and strain in elasticity theory. Stress is not a physically measurable variable, but is the driving function that produces the physically measurable strain.

The algebraic-propagation-model block has no dynamics and, consequently, the developed phase, ψ_h, is an instantaneous output function of the input variables. However the actual phase, $\bar{\psi}_h$, does not develop instantaneously, and is related to the developed phase by a lag caused by the beam heating dynamics.

38
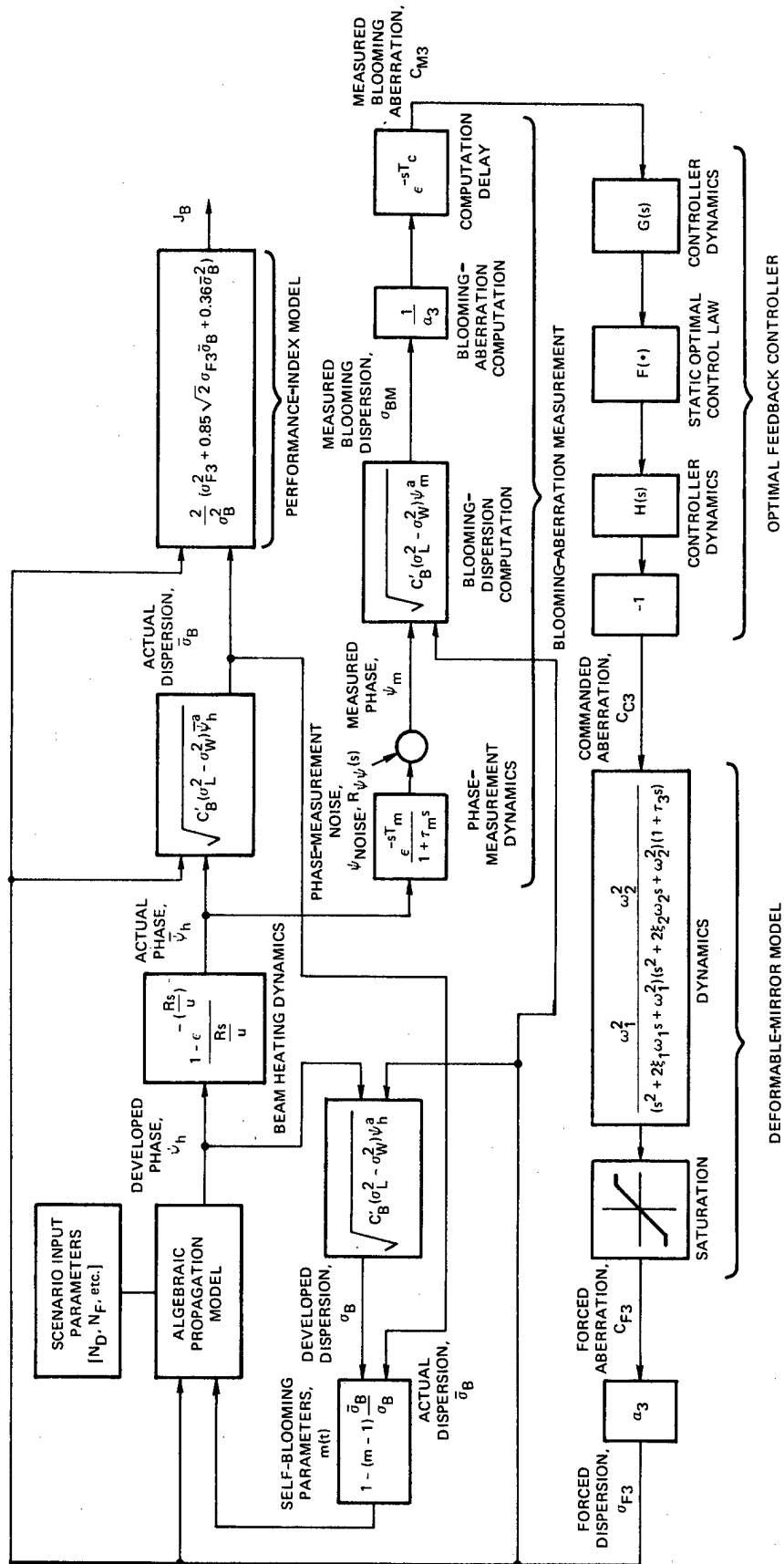
Figure 29. Dynamic closed-loop model of thermal blooming.

Table 1. Constants and variables for the dynamic control model.

Variable/Constant	Description
Scenario Parameters:	
N_D	Distortion number
N_F	Fresnel number
N_Q	Laser quality number
T	Transmission
$D \left(= \dfrac{\sqrt{2}\pi m'M}{m''} \right)$	Parameter grouping
C_B'	Beam descriptor
a	Beam descriptor
m'	Beam descriptor
m''	Beam descriptor
R	Aperture radius
v	Transverse wind velocity
Blooming-Process Variables:	
s	Laplace transform variable
ψ_h	Developed heating phase
$\overline{\psi}_h$	Actual heating phase
σ_B	Developed blooming dispersion
$\overline{\sigma}_B$	Actual blooming dispersion
m(t)	Self-blooming parameter
Aberration-Measurement Variables:	
T_m	Phase-measurement computation delay
τ_m	Phase-measurement time constant
ψ_{noise}	Phase-measurement noise

Table 1. Constants and variables for the dynamic control model. (Cont.)

Variable/Constant	Description
Aberration-Measurement Variables: (Continued)	
$R_{\psi\psi}(s)$	Phase-measurement noise PSD
σ_{BM}	Measured blooming dispersion
C_{M3}	Measured blooming aberration
T_c	Computational delay
Deformable-Mirror Variables/ Constants:	
$\omega_1,\ \omega_2$	Mirror dynamics constants
$\xi_1,\ \xi_2$	Mirror dynamics constants
τ_3	Mirror dynamics constant
C_{C3}	Commanded blooming-aberration input
C_{F3}	Aperture-forced blooming-aberration output
σ_{F3}	Aperture-forced dispersion output
Optimal-Feedback-Controller Variables:	
C_{M3}	Measured blooming-aberration input
C_{C3}	Commanded blooming-aberration output
Performance-Index Variables:	
σ_D	Diffraction limit
σ_{F3}	Focus dispersion forced at the aperture
$\bar{\sigma}_B$	Actual blooming dispersion

The transfer function for this dynamic block is derived below. The time domain relationship for the actual phase, $\psi_h(t)$, in terms of the developed phase, $\bar{\psi}_h(t)$, is

$$\bar{\psi}_h(t) = \frac{1}{R} \int_0^R \psi_h\left(t - \frac{r}{v}\right) dr \qquad (5)$$

where R is the radius of the aperture, v is the transverse wind velocity, and r is the radial distance in the aperture. This equation models the beam heating dynamics of convective heat transport, and neglects thermal diffusion. Equation (5) is Laplace transformed to yield

$$\bar{\Psi}_h(s) = \frac{1}{R} \int_0^R \epsilon^{-rs/v} \Psi_h(s) \, dr$$

where s is the Laplace transform variable, and the Laplace transform is denoted by capital letters $\bar{\Psi}_h$ and Ψ_h.

Since $\Psi_h(s)$ is independent of the variable of integration, a simple rearrangement provides the expression for the dynamic transfer function

$$\frac{\bar{\Psi}_h(s)}{\Psi_h(s)} = \frac{1}{R} \int_0^R \epsilon^{-rs/v} \, dr \qquad (6)$$

Integration of Eq. (6) provides the transfer functions shown in Figure 30.

$$\text{DEVELOPED PHASE, } \psi_h \longrightarrow \boxed{\dfrac{1 - \epsilon^{-(rs/v)}}{\left(\dfrac{rs}{v}\right)}} \longrightarrow \text{ACTUAL PHASE, } \bar{\psi}_h$$
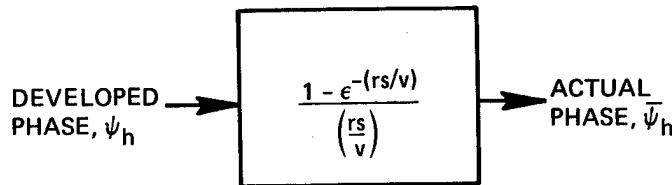
Figure 30. Beam heating dynamics.

42

It is noted that the transport lag time and integrator gain are both dependent on the transverse wind velocity, v, in the same manner. The limiting form of this transfer function for large and small values of v is

$$\text{For large v:} \quad \frac{1 - \epsilon^{-(rs/v)}}{\left(\dfrac{rs}{v}\right)} \rightarrow 1$$

$$\text{For small v:} \quad \frac{1 - \epsilon^{-(rs/v)}}{\left(\dfrac{rs}{v}\right)} \rightarrow \frac{v}{rs}$$

It is seen that for large wind velocities, the beam heating dynamics have the limiting form of a simple gain of 1, i.e., no dynamics. For small wind velocities, the dynamics approach a low gain integrator. However, for very low wind velocities, thermal diffusion may not be negligible and corrective terms may be required.

In addition to including a heating-phase dispersion term, the algebraic propagation model also employs beam dispersion terms. Consequently, the relationship between heating-phase and beam dispersions appears in the thermal-blooming model. This relationship is a non-linearity that results from a straightforward application of the algebraic propagation model, and appears in Figure 31. Three blocks of this type appear in the process model.
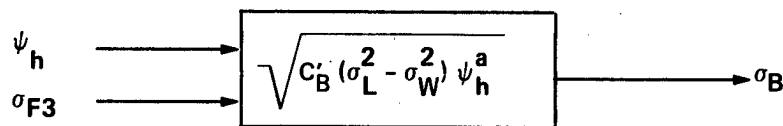
Figure 31. Heating-phase beam-dispersion model.

43

The remaining block in the thermal-blooming process is the model for the self-blooming parameter. This parameter models the time-varying effect of thermal blooming on itself, and is shown in Figure 32. Appropriate interconnection of the blocks described results in the thermal-blooming-process model shown in Figure 29.

DEVELOPED DISPERSION
σ_B ⟶

$$1 - (m - 1)\frac{\bar{\sigma}_B}{\sigma_B}$$

$m(t)$ ⟶ **SELF-BLOOMING PARAMETER**

ACTUAL DISPERSION
$\bar{\sigma}_B$ ⟶
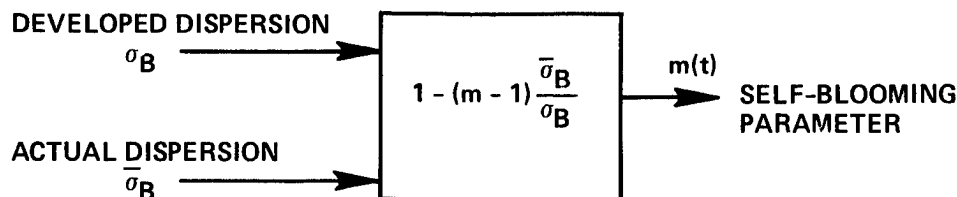
Figure 32. Self-blooming parameter model.

5.2 Aberration-Measurement Block

The aberration-measurement model for the dynamic case must allow for lags due to measurement sensors and computational delays. In addition, measurement noise is allowed dynamic characteristics and modeled with a PSD. A further measurement complication is that the optical aberration due to thermal blooming and the aberration forced at the aperture by the deformable mirror interact in a nonlinear manner. Consequently, a computation involving the aberration forced at the aperture is required in order to separate the blooming effect. In the dynamic model, this computation introduces a short time lag.

The aberration-measurement block appears in Figure 33. The sensor lag is modeled as a simple lag with a time constant, τ_m, in conjunction with a computational delay, T_m. The computational delay appears in the preconditioning calculations of the phase measurement. It is possible that this measurement is in the form of sampled data. This effect is easy to model, but is not included at this time.

44
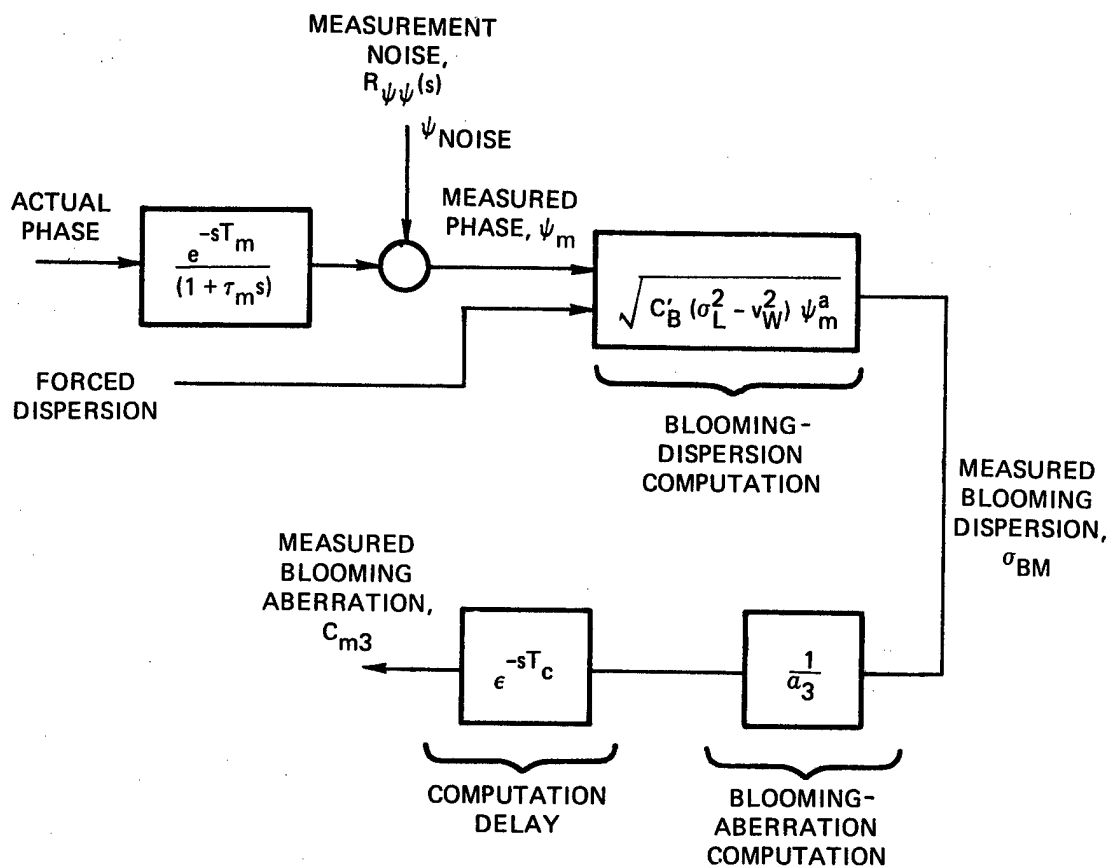
Figure 33. Measurement dynamics model.

Measurement noise with a PSD of $R_{\psi\psi}(s)$ is added to the measure-
ment, and is followed by a nonlinear computation involving the aberration
forced at the aperture. This computation introduces another delay, T_c,
resulting in the final measurement, C_{M3}. The measurement model indicated
in Figure 33 is flexible, and changes are easily introduced to adapt the
model to particular systems. Consequently, unlike the physical blooming
process, this model is alterable, and can be modified according to the
particular system under study.

45

5.3   Deformable-Mirror Block

The deformable mirror is the phase modifier that provides corrective action at the aperture. At the present time, high-power deformable mirrors are not well developed in terms of spatial and temporal performance (see Section 6). Since the deformable mirror is an alterable component in the system design, the approach taken in this modeling effort is to model an existing high-power mirror.[5] This approach allows the current mirror dynamic shortcomings to be made visible and provides a basis for departure to a more acceptable mirror design. The dynamic model includes the following effects:

(1)   Voice coil drive: first-order lag, τ.

(2)   Movable mass spring: second-order lag, ω_1, ξ_1.

(3)   Mount compliance dynamics: second-order lag, ω_2, ξ_2.

In addition to these dynamics, mirror saturation nonlinearity is included in the model.

Figure 34 shows the deformable-mirror block, with provision for including the effect of base vibration. Base vibration is not modeled at the present time, but may be important in future studies.

COMMANDED ABERRATION

$$\frac{\omega_1^2 \, \omega_2^2}{(1 + \tau s) \, (s^2 + 2\xi_1 \omega_1 s + \omega_1^2) \, (s^2 + 2\xi_2 \omega_2 s + \omega_2^2)}$$

DYNAMICS

SATURATION

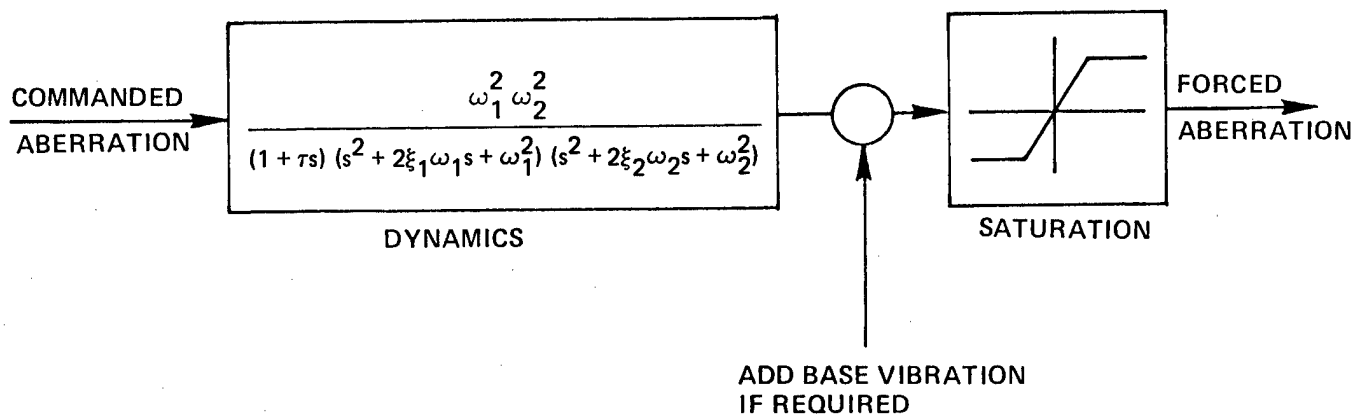FORCED ABERRATION

ADD BASE VIBRATION IF REQUIRED

Figure 34.   Deformable-mirror-dynamics model.

46

5.4 Optimal-Feedback-Controller Block

The optimal feedback controller consists of the static optimal
control law plus compensation for dynamic effects. There are many
possible configurations for putting dynamics in the controller, and it
is desired to choose the simplest overall system configuration. The
controller dynamics must compensate for: beam heating dynamics, measure-
ment dynamics, and deformable-mirror dynamics.

A controller configuration that will perform this function appears
in Figure 35. The reason for two dynamic compensation blocks is that
transfer functions are not commutable with the nonlinearity, $F(\cdot)$. Since
dynamic compensation is simply control logic, it is an easy matter to
put control logic on either side of the nonlinearity.

MEASURED
ABERRATION → [G(s)] → [F(Y)] → [H(s)] → [-1] → COMMANDED
ABERRATION

Measurement   Optimal   Mirror
Compensation   Static   Compensation
Dynamics   Nonlinearity   Dynamics
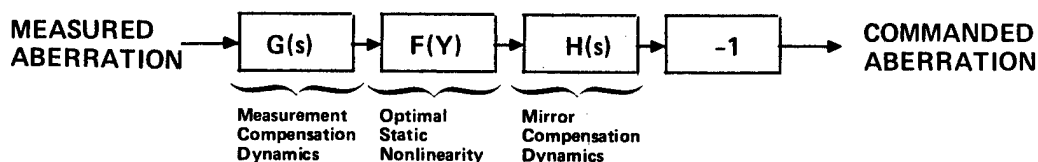
Figure 35. Optimal feedback conroller.

Inspection of Figure 29 indicates that the only unalterable
dynamics in the system are the beam heating dynamics; the measurement
and deformable-mirror dynamics may be changed. However, the beam heat-
ing dynamics are relatively mild and can be controlled with a simple
dynamic compensator. Measurement dynamics are also not severe, and
dynamic compensation is relatively easy. However, the dynamics of
the existing deformable mirror are severe, and require extensive
compensation.

47

In general, an integrated optimal controller design can only be achieved by modifying the measurement dynamics and deformable-mirror dynamics while developing the dynamic compensation. In this particular case, i.e., for the HEL, it is clear that the bulk of dynamic compensation must be applied to the deformable mirror, and not to the thermal-blooming process. An integrated system approach would be to redesign the deformable mirror so that mirror dynamic compensation would be consistent with the remainder of the control system. Consequently, it is recommended that measurement and deformable-mirror dynamics be altered, along with the design of the dynamic compensator, to achieve a balanced controller configuration. In addition, it is recommended that the controller and deformable mirror be designed together in an integrated manner consistent with the Army scenario as a means of optimizing the overall controller configuration.

5.5 Performance-Index-Model

The performance index for the dynamic model is the same as for the static case (refer to Figure 27). This model in the unnormalized form appears in Figure 29.

5.6 Uses of the Dynamic Control Model

Dynamic control analysis consists of several possible tasks. One task would be to analyze the static null stability of the proportional control loop, i.e., generalized phase-conjugate correction, and compare the results of the analysis with what is known behavior for such loops. This is a sort of validation exercise, although not complete, for the dynamic control model. Additional tasks related to development of the beam controller are as follows.

Dynamic feedback controller design is accomplished by synthesizing compensators G(s) and H(s) such that the closed-loop system is stable and has the desired transient response in terms of the thermal-blooming

48

performance index, J_B. Upon completion of the controller design, specifications for the measurement noise and measurement dynamics can also be made in terms of J_B. That is, one can set specifications on $R_{\psi\psi}$, τ_m, T_m, and T_c in terms of the loss of intensity on target, J_B. If the loss in intensity on target is very small, then the measurement system is too good, and hence too expensive. Conversely, if the loss in intensity is too large, then the measurement system is inadequate.

A similar exercise can be done in terms of the deformable-mirror bandwidth and saturation level. As a result, it is seen that proper use of this dynamic model would allow for design of the HEL beam controller in an integrated and self-consistent manner.

SECTION 6

PULSED ADAPTIVE-OPTICS DEFORMABLE MIRROR

For proper phase correction, a pulsed adaptive-optics deformable mirror requires a different set of Zernike mode shapes from a continuous-wave deformable mirror. In Reference 6,[*] an analysis of actuator design considerations for the continuous-wave case showed that a continuous-wave deformable mirror consisting of a plate could be made to assume the shape of an arbitrary linear combination of eight Zernike modes.

In Reference 6 it was also shown that actuators must perform three functions: pressure loading on the back of the plate, edge control via shear forces and bending moments, and proper positioning of the outer plate edge with respect to the optical reference plane. All Zernike modes except spherical aberration require zero pressure load on the back of the plate. For spherical aberration, a uniform pressure load is required. The major portion of actuator action was found to be concentrated in the bending moments and shear forces at the boundary. Consequently, proper boundary control is essential and expressions for actuator boundary control requirements were developed.

---

[*] Reference 7 also contains information pertinent to adaptive-optics deformable mirror requirements. For convenience, both References 6 and 7 are abstracted in Appendix B.

The mirror deformation required for proper phase compensation of pulsed-laser beam aberrations is given by Eq. (6) of Reference 8.[*] The equation is reproduced here for convenience:

$$\psi_c = N \left\{ 0.317 + 0.485x - 0.111(x^2 + y^2 - 0.5) + 0.223(x^2 - y^2) \right.$$
$$+ 0.043x(x^2 - 3y^2) - 0.028x(3x^2 + 3y^2 - 2)$$
$$- 0.003\left[6(x^2 + y^2)(x^2 + y^2 - 1) + 1\right]$$
$$\left. + 0.020\left[4(x^4 - y^4) - 3(x^2 - y^2)\right] - 0.023(x^4 - 6x^2y^2 + y^4) \right\}$$

$$(7)$$

Equation (7) is a fourteenth-order Zernike mode expansion of the required mirror shape. However, since the shape is symmetric about the wind-direction axis, only nine terms appear in the expansion.

It was further found in Reference 8 that variation of the scenario parameters, with the exception of wind direction, did not result in a change of deformation shape, but only scaled the amount of the shape given by Eq. (7). The axis of symmetry in the mirror shape must lie along the wind-direction vector. Consequently, the pulsed adaptive-optics deformable mirror must conform to the shape expressed by Eq. (7), with a scalable amount of deformation, and provide for a rigid-body rotation (about the optical axis) of the shape for proper orientation with respect to the wind.

Since the basic shape of the mirror does not change in distribution, but only in magnitude, a reduction in actuator complexity can be achieved. The requirements for the continuous-wave mirror were to take the shape of a nine-term Zernike mode expansion with arbitrary

---

[*] For convenience, Reference 8 is included in this report as Appendix C.

51

variation in the expansion coefficients. Consequently, the actuators for the continuous-wave mirror must be able to force the mirror into eight separate independent shapes (translation is excluded as a shape).

In the pulsed case, the expansion coefficients are fixed and the actuators need force only one shape on the mirror, not eight separate ones. However, it must be possible to rotate this shape about the optical axis in a rigid-body manner. Although it is always possible to physically rotate the entire mirror assembly to achieve this, a more attractive alternative is presented.

The difference between the Zernike mode expression given in Eq. (7) and the Zernike modes analyzed in Reference 8 is the addition and deletion of a few modes. Consequently, it is easy to extend the previous analysis to apply to the pulsed-laser mirror.

The actuator requirements are separated into three areas:

(1)   Orientation of plate with respect to the optical plane.

(2)   Boundary shear forces and bending moments.

(3)   Plate pressure loading.

The first requirement applies to the rigid-body orientation of the plate, which consists of tilt and translation. The requirement is unchanged for the pulsed-laser adaptive-optics case.

To meet the second requirement, actuators producing shear force and bending moments are introduced at the edge of the plate. The analysis in Reference 6 indicates that these shear forces and bending moments must vary in magnitude with the azimuth angle θ according to formulas generated from the Zernike mode expressions.

Again, this requirement remains unchanged, since most of the Zernike modes of the Reference 8 analysis are included in the expansion of Eq. (7). The actuator array producing these shear forces and bending moments must be simplified for the pulsed-laser mirror case,

since the actuators have to force only one set of forces and moments instead of eight independent sets. Consequently, a considerable simplification in actuator requirements occurs in this area.

The requirement of pressure loading on the plate requires further analysis of the new Zernike terms. The pressure load required for the mirror is proportional to ∇^4 operating on the surface deformation.[6] Consequently, a calculation of ∇^4 operating on each term of Eq. (7) will provide an indication of the pressure load required. This pressure load computation appears in Table 2.

Table 2. Plate pressure load requirements.

Zernike Mode	Plate Pressure Load
1	0
x	0
$x^2 + y^2 - \dfrac{1}{2}$	0
$x^2 - y^2$	0
$x^3 - 3xy^2$	0
$x(3x^2 + 3y^2 - 2)$	0
$6(x^2 + y^2)(x^2 + y^2 - 1) + 1$	384
$4(x^4 - y^4) - 3(x^2 - y^2)$	0
$x^4 - 6x^2y^2 + y^4$	-24

It is seen from Table 2 that only two modes require a pressure load on the plate, and that both of these pressure loads are uniform. Consequently, they could easily be implemented via a pressurized fluid, rather than with many disjoint forcing devices.

Since the two pressure terms differ in sign, the possibility of cancellation occurs. The net pressure is found from weighting the pressure loads in Table 2 with the appropriate coefficients from Eq. (7)

$$P_{net} = 0.003(384) + 0.023(-24)$$

$$= 1.15 - 0.55 = 0.60$$

It is seen that a net positive uniform pressure is required on the mirror to achieve the proper shape. Furthermore, since 0.60 is not small with respect to 1.15 or 0.55, the magnitude of the net pressure load may not be negligible. However, before drawing any conclusion regarding the necessity of the pressure load on the mirror, it is recommended that the error incurred from deleting these two terms be assessed.

Currently, the curve fit of Eq. (7) to the required shape is accurate to 10 percent. The two modes requiring pressure loads on the back of the mirror are not dominant terms and tend to cancel. Consequently, it may turn out that deleting these two terms from the required shape would only increase the error a few percent, resulting in no pressure-load requirement on the mirror. This would constitute a trade condition from the viewpoint of engineering the deformable mirror.

At this point, the physical dimensions required for the mirror deflection are computed. The worst-case phase compensation of ±20 radians is taken from Reference 8. This corresponds to ±3.18λ of phase error. For λ = 10.6 micrometers, this corresponds to a deflection of ±1.3 × 10^{-3} inches. Since only one half of this deflection is required at the mirror, then a physical mirror deflection of ±0.65 × 10^{-3} inches is required.

Since the actual mirror may be 5 to 10 inches in diameter, it is seen that the peak deflections are well within the small deflection range required by the mathematical theory of elasticity used in this analysis.

At this point, the requirement of orienting the mirror shape with respect to the wind direction is considered. The specific shape described by Eq. (7) was computed for the case where the wind direction is aligned with the target velocity vector. It has been found that the expansion coefficients in Eq. (7) do not change for target velocity directions up to ±45 degrees away from the wind direction, if a rigid-body rotation is applied to align the mirror shape with the wind direction.[8] Consequently, an actuator requirement is to provide the capability of rotating the shape of the mirror about the optical axis.

In order to provide this rotation capability without physically rotating the mirror, which is a slow cumbersome process, an alternative scheme is recommended. It is first observed that if a uniform pressure is required on the back of the mirror, and this might not be the case, then a uniform pressure is invariant under a rotation about the optical axis, and no impact on these actuator requirements results. Consequently, there is no change of the pressure-load distribution required to achieve this rotation. Similarly, it can be seen that a rotation about the optical axis would have no impact on the rigid-body orientation actuators controlling translation and tilt.

The remaining actuator requirement of providing forces and moments at the mirror boundary is now examined. Actuators must provide shear forces and bending moments along the plate edge in a manner derived in Reference 6. However, only one set of actuators is needed for the pulsed-laser mirror. It is proposed that another set of actuators providing the forces and moments be placed on the plate, but with a physical rotation of 90 degrees about the optical axis.

55

This second set of actuators would provide the same shear forces and bending moments on the plate, but with a rotation of 90 degrees in position. If these two sets of actuators are now driven with a cos θ weighting of the first set and a sin θ of the second set, then the result provides a rigid-body rotation of the entire shape on the mirror through an angle θ about the optical axis. Thus, for wind direction changes of up to ±45 degrees with respect to the target velocity vector, adequate compensation can be achieved via a rigid-body rotation of shape on the mirror. This effect is diagrammed in Figure 36.
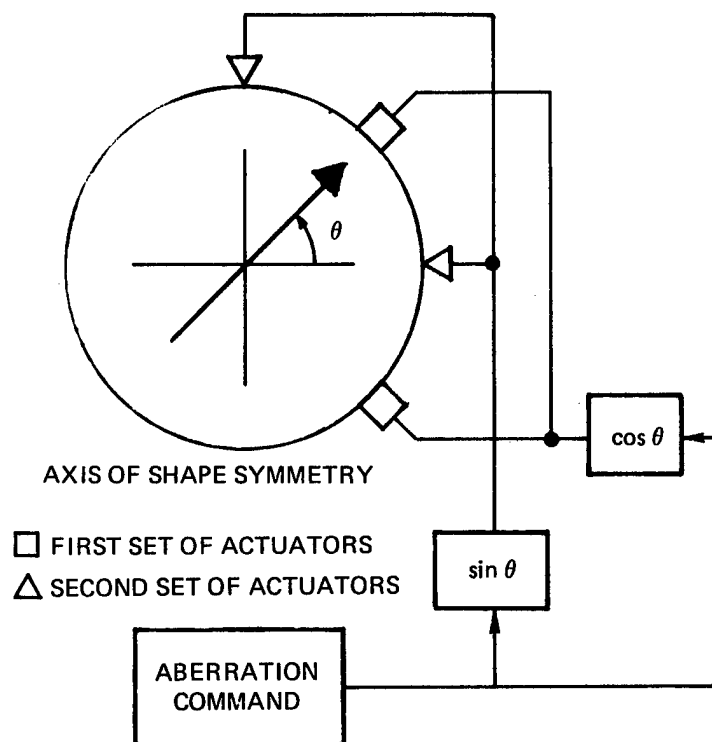
Figure 36. Pulsed-laser mirror-shape rotation.

In summary, the fact that the shape of the mirror need not change, but only be scaled in magnitude and rotated, provides considerable actuator requirement simplification. However, the question arises: Does the ±45-degree alignment envelope cover all of the scenario cases? If not, then further work must be done to determine the required phase profile and mirror shape, along with the corresponding impact on mirror actuator requirements.

SECTION 7

SUMMARY

It has been demonstrated that the controller structure appearing in Figure 7 has the potential for the best beam-controller performance. Since the beam-control problem is quite difficult, it is recommended that this dual-control-loop structure be employed in the HEL phase-control system.

The algorithm for the closed-loop control of atmospheric effects operates on phase measurements, and produces a command to a phase corrector. The algorithm provides dynamic compensation for proper closed-loop stability, and issues a command to the phase compensator that is almost a phase-conjugate correction. A special correction is applied for the focus due to thermal blooming.

The phase information necessary for the algorithm consists of a wide-band phase measurement, a time-domain low-pass filter, a spatial focus filter, and appropriate interconnections. A spatial blooming filter may also be required for the region of turbulence and focus spectral overlap, but this requirement has not been determined at this time.

The algorithm for special thermal-blooming focus correction was first investigated for the static case. A model of the physical thermal-blooming process (algebraic model), phase measurement, optimal static control algorithm, phase corrector, and performance index was developed and appears in Figure 28. This model can be used to develop the

optimal static thermal-blooming control law. Other uses of the model of the static closed-loop beam controller are to generate measurement-system and deformable-mirror requirements and specifications.

The real-time operation of the closed-loop beam controller requires appropriate dynamic compensation in the focus blooming control algorithm. In order to develop the dynamic compensator, a dynamic model of the blooming process and controller was developed and appears in Figure 29. Uses of this dynamic model are similar to those of the static model, but in addition include dynamic compensation and dynamic specifications for the measurement system and phase corrector.

Key hardware development requirements are identifiable from the analyses so far presented. To begin with, the dual-loop structure requires development of an HEL beam sampler for use with the high-power adaptive mirrors, or some alternative form of beam cleanup.

One alternative would be a nonlinear phase conjugator. However, phase conjugators are in the early stage of development and, consequently, it is a long time before their use at the high-power level will become feasible. Furthermore, in keeping with the dual-loop control philosophy, a laser with phase conjugator could be used for beam cleanup in the structure as shown in Figure 6. The phase conjugator could not be used for atmospheric correction, as could a high-power adaptive mirror, because phase conjugation will not be stable for that loop. Consequently, even if phase conjugators do become operational, deformable mirrors would still be required for correcting the atmospheric disturbances in a dual-loop structure.

High-power adaptive mirrors represent a technology which simply has not been done right; the needed approach is described in Reference 6 and 7. For the pulsed case, the requirements are particularly simple, as described in Section 6.

APPENDIX A

THERMAL-BLOOMING-PROCESS MODEL

Because the derivation of the thermal-blooming-process model consists of a long sequence of lengthy algebraic manipulations, only an outline of the key steps is presented here (see Reference 1).

The first step is to normalize the variables. X is the normalized control aberration forced at the aperture. Y is the normalized aberration from thermal blooming. σ_D is the diffraction limit.

$$X = \frac{\sigma_{F3}}{\sigma_D}$$

$$Y = \frac{\sigma_B}{\sigma_D}$$

The derivation starts with the algebraic expression for the heating phase, ψ_h.

$$\psi_h = \left[\frac{N_D N_F N_R}{N_Q' A} \right] e^{-(\varepsilon z_t)/2} \ln \left| \frac{(N_S + N_R + A)(N_S + 1)}{-B N_R + N_S + N_R + AC} \right|$$

The derivation continues by application of algebraic manipulations, ending with the modified expression

$$\psi_h = \frac{N_D N_F T}{\sqrt{1 + 2X^2}} \ln \left| \frac{\left(\dfrac{2N_F}{D} \right)}{X + \sqrt{X^2 + \left(\dfrac{2N_Q}{D} \right)^2 \left(\dfrac{N_F}{D} - X \right)^2}} \right|$$

Continuing with further algebraic model relationships

$$\sigma_B = \sqrt{C_B' \left(\sigma_L^2 - \sigma_W^2\right) \psi_h^a}$$

$$\sigma_L^2 - \sigma_W^2 = \sigma_D^2 + 2\sigma_{F3}^2$$

we arrive at the final result shown in Figure 2.

$$Y = \sqrt{C_B' \left(N_D N_F T\right)^a} (1 + 2X^2)^{(2-a)/4} \ln^{a/2}(\cdot)$$

APPENDIX B

ABSTRACTS OF
REFERENCES 6 AND 7
(CSDL REPORTS C-5065 AND C-4990)

B.1   Reference 6 (C-5065): Actuator Design Considerations for
       a Deformable Mirror

The optical modes considered in this analysis are the Zernike modes:
translation, tilt, focus, astigmatism, coma, and spherical aberration.

Actuator requirements were derived for perfect deformation of a
uniform circular plate into the shape of the Zernike modes. Actuator
requirements were separated into two groups: those acting over the
surface of the plate and those acting only on the outer plate boundary.

For perfect static deformation of the plate into the shape of a
Zernike mode, it was found that no actuators were required on the surface
of the plate except for the case of spherical aberration. The surface
actuator requirement for spherical aberration was found to be that of
a uniform pressure over the plate surface. In all of these cases
except one, no plate surface actuators were required to achieve the
ideal static shape of a Zernike mode. In conforming to the shape of
a Zernike mode, considerable flexing (rigid body modes excepted) of
the plate takes place.

The aforementioned two considerations indicate that most of the
actuator influence appears at the plate boundary, and attention was
focused in this area. In general, it was found that actuator boundary
requirements consisted of relatively simple bending moments and shear

forces. Under the action of these actuator requirements, the plate is in static equilibrium. The remaining boundary actuator requirement was found to be a rigid body motion to properly position the outer edge of the plate with respect to the optical reference plane. Since plate boundary conditions were found to be the main influence in actuator requirements, the case of a uniform tension or compression of the boundary was also examined. The presence of this force complicated actuator requirements considerably and this situation should be avoided by mechanical design.

Similarly, variation in plate thickness led to a complicated increase in actuator requirements and offered no advantage. After a thorough treatment of static actuator requirements, plate dynamics and dithered Zernike modes were introduced. Dynamic actuator requirements were obtained and the subject of structural resonances was treated. Again, it was found that the actuator requirements were relatively simple in terms of structural loading requirements.

In summary, relatively simple structural loading, mainly at the boundary, of a plate can result in perfect deformation to the shape of a Zernike mode. A review of existing deformable mirror actuator configurations indicates that critical structural loading requirements are not being met by present designs.

B.2   Reference 7 (C-4990): A Method for Improving the Performance of High-Energy Adaptive-Optics Deformable Mirrors

Deformable mirrors were originally developed for imaging applications, and consisted of an array of disjoint segmented mirrors, each mounted on a piston actuator. Engineering considerations for this configuration grew to favor stiff position transducers in the actuator array; the actuator geometry was determined by the segmented-mirror array where each piston mirror is positioned independently. This actuator array and transducer assembly were highly successful in deforming the segmented mirror for imaging purposes.

The extension of deformable-mirror technology to high-energy applications led to the use of plates for the mirror substrate. In spite of the fact that a plate has a very different structure from a segmented array of mirrors, the segmented-mirror actuator design was retained. Similarly, the requirement for noninteraction of the segmented piston actuators was also retained. Since any physically realizable force pattern on a plate cannot produce a deflection remotely approximating a segmented piston, the ability of the mirror to deform to an optical shape was altered considerably. The result is the current state of technology, where high-energy-application performance is significantly below that obtained in imaging applications.

The high-energy-system performance limitations caused by the presently employed deformable-mirror structural model arise not from the mirror physics but from the manner in which interactuator coupling is treated. The model is formulated according to the principle of actuator command signal superposition, and current designs are based on the line of thought that interactuator coupling is undesirable because it causes error coupling between the various control loops involved. In fact, considerable effort has been expended to reduce interactuator coupling to a small value by designing actuators to be very stiff springs in the uncommanded state. However, reduction of interactuator coupling as a goal in itself severely limits the ability of the high-energy mirror to properly deform to the shape of an optical mode, and further reduction of actuator coupling or the addition of more actuators will further degrade the present level of performance. Clearly, a different approach to structural modeling is in order.

If interactuator coupling is viewed as beneficial and it is used advantageously in deforming the mirror to the desired shape, then a new structural model is obtained which will improve high-energy-system performance. Calculations[*] indicate that a high-energy mirror designed according to this new mirror structural model will provide error-free performance.

---

[*] Reference 5 of Reference 7.

65

APPENDIX C

REPORT ON
A THEORETICAL ANALYSIS OF
ADAPTIVE OPTICS FOR
REPETITIVELY PULSED LASERS*

Theoretical Analysis of Adaptive Optics for Repetitively Pulsed Lasers

James Wallace

Far Field, Inc., Sudbury, Massachusetts 01776

In this report we determine the mirror contours that compensate for thermal blooming of a repetitively pulsed laser at 10.6 μm. In particular the effects of wind speed, wind direction, absorption coefficient, range and altitude dependence are discussed. The major conclusion reached is that the normalized mirror contours are insensitive to a factor of two change in all variables except the wind direction. An expansion of the phase in Zernike polynomials is also presented and compared to the numerical results. The largest terms in the expansion are the tilt, refocus and astigmatic corrections. A factor of ten increase in the irradiance can be achieved with the use of adaptive optics.

I. INTRODUCTION

Compensating for thermal blooming of repetitively pulsed lasers can achieve factors of ten increase in the irradiance at the focal plane. To realize this potential the pulse repetition frequency must be chosen so that the density gradients from the previous pulses do not overlap in the depth of focus. It then becomes important to determine how the mirror contours depend upon the local atmospheric conditions. The answer to this question impacts on the type of system and the number of mirror actuators required to implement adaptive optics.

Results for the mirror contours are presented that, for the high slew rates expected in Army HEL applications, the normalized mirror contours are relatively insensitive to a factor of two change in wind speed, range, slew rate, and absorption coefficient. Local atmospheric conditions primarily affect the overall value of the mirror deflection and not the distribution. Since the normalized mirror contours are reasonably fixed an accurate analytic expression is also presented. This is based upon an expansion in Zernike polynomials and is carried out with sufficient accuracy so that it can be regarded as exact. A second analytic result gives the normalization value that is valid for both horizontal and vertical propagation in the atmosphere.

Results for the irradiance are presented and compared to the blooming results. Results for only the lowest order corrections are also compared to the blooming results. The conclusion reached is that, for Army applications of HEL systems, adaptive optics can increase the irradiance by an order of magnitude.

II. DETERMINATION OF THE MIRROR CONTOURS

In the optical-frequency range, Maxwell's equations can be approximated by the paraxial approximation to the scalar wave equation. The electric field is taken to be of the form

$$E = A(x, y, z)\exp(ikn_\infty z - \alpha z/2),\tag{1}$$

where x and y are the coordinates transverse to the propagation direction z, α is the absorption coefficient, n_∞ is the index of refraction in the atmosphere, and k is the wave number. The diffracted amplitude A is complex and the irradiance I is defined as EE*. The governing equation, in normalized variables x/R_m, y/R_m, z/z_f is

$$2iFn_\infty A_z + \nabla^2 A + 2k^2(n_\infty-1)R_m^2 \rho A = 0,\tag{2}$$

where R_m is the radius of the aperture, ρ is the density perturbation caused by heating, z_f is the distance to the focal plane and F is the Fresnel number kR_m^2/z_f. For a beam focused at z_f, the appropriate boundary condition at z=0

$$A = A_o(x, y, 0)\exp[iF(\psi^c(x, y)-(x^2+y^2)/2)].\tag{3}$$

The phase ψ^c is chosen to minimize the effects of atmospheric heating and is the negative of the optical phase determined by propagating a point source from

the geometric focal point to the aperture. In a coordinate system converging to the geometric focal point the governing equation is

$$-\psi_z + [(\psi_\xi)^2 + (\psi_\eta)^2]/2(1-z)^2 = z_f^2 (n_\infty - 1)[\rho(\xi(1-z), \eta(1-z), z)]/R_m^2, \qquad (4)$$

where $\xi = x/(1-z)$, $\eta = y/(1-z)$ and $\psi = 0$ at $z = 1.0$. For thermal blooming of repetitively pulsed lasers the steady state density is related to the irradiance by

$$\rho = -\exp(-\alpha z)\left(\frac{(\gamma-1)\alpha I_a t_s}{\gamma p_\infty}\right)\sum_{n=1}^{\infty} I(x-U_x(z)t_s n/R_m, y-U_y t_s n/R_m, z) \qquad (5)$$

where α is the absorption coefficient, $\gamma = 1.4$ is the ideal gas constant, I_a is the average power at the laser, p_∞ is the pressure, $U_x(z)$ is the z dependent velocity in the x-direction, and U_y is the wind velocity perpendicular to the beam motion. The interval between pulses, t_s, is determined from the pulse repetition frequency. The mirror contours are determined by substituting Eq. (5) into Eq. (4) and simultaneously solving Eqs. (2) and (4).

We now present results for a repetitively pulsed laser at 10.6 μm with a power of 1MW, an absorption coefficient of 0.236/km, and a wind velocity in the direction of the beam motion. In Fig. 1 the beam is focused at 3 km and has a transverse component of velocity of 110 m/s at the focal plane. The profiles of the phase distribution in the x or transverse flow direction are shown for 4 scans perpendicular to the transverse flow. In Fig. 2 the beam is focused at 5 km with a velocity of 67 m/s at the focal plane. The phase distribution in both

figures can be compared by overlaying the results and changing the scale of ψ_c to unity. The normalized phase distributions are nearly identical except for a small difference in the downstream or positive x direction. This difference is due to the fact that, in Fig. 2, the velocity at the focal plane is significantly less than that of Fig. 1. This increases the length of the atmospheric lens and the additional path length is heated by an irradiance that differs from that of Fig. 1. However these two cases represent the maximum difference that will occur in Army applications of HEL systems and even this difference is acceptable small. Only the displacement of the mirror at the centerline exhibits any significant dependence upon the local atmospheric conditions. Actual implementation of adaptive optics will then be simplified since point to point measurements of the blooming phase are not required.

An accurate analytical result for the optical phase can be determined by expanding the numerical results in a Zernike series. This gives the following expansion for the phase.

$$\psi_c = N\left\{0.317 + 0.485x - 0.111(x^2+y^2-0.5) + 0.223(x^2-y^2) + 0.043x(x^2-3y^2) - 0.028x(3x^2+3y^2-2) - 0.003(6(x^2+y^2)(x^2+y^2-1)+1) + 0.020(4(x^4-y^4)-3(x^2-y^2)) - 0.023(x^4-6x^2y^2+y^4)\right\}.$$

(6)

The major components of the phase distribution are the refocus and astigmatism terms. Addition of these two terms indicate that the compensating phase has a tilt and defocus component in the x-direction and a focus component in the y-direction. The analytical results are shown in Fig. 3 and give an almost exact

73

fit to the numerical results over a range of absorption coefficients, wind speed and slew rates. This is more clearly seen by overlaying the results given in Fig. 3 with those shown in Figs. 1 and 2. The normalization constant, N, is determined from the value of the phase at the centerline $x = 0$, $y = 0$. Variations in the wind speed, absorption coefficient, and slew rates primarily affect the distortion parameter N rather than the phase distribution.

The above results are for sea level propagation. A variable atmosphere also changes the normalization constant N. To incorporate the altitude dependence of the absorption coefficient we will use the Euler-Maclaurin summation formula to obtain an analytical representation of the density given by Eq.(5). This results in

$$\sum_{0}^{N_p-1} f(n) \cong \int_{0}^{N_p} f(n) \, dn - 0.5(f(N_p) - f(0)) + 0.0833(f'(N_p) - f(0)) - 0.0014(f'''(N_p) - f'''(0)),$$

$$(7)$$

where $N_p(z) = D(z)/U(z)t_s$ and $f(n) = I(x - 2(n+1)/N_p(z), y, z)$. Integrating the density from $z = 0$ to $z = z_f$ and evaluating the result at $x = 0$, $y = 0$ gives the normalization parameter N as

$$N \cong k(n_\infty - 1) \left(\frac{(\gamma - 1)I_a t_s}{\gamma p_\infty} \right) \int_{0}^{z_f} \left\{ \alpha(z') \exp(-\int_{0}^{z'} \alpha(z'') dz'')/U(z')R(z') \right\} \left\{ \int_{-\infty}^{-2/N_p} I(u) \, du + \right.$$

$$\left. I(-2/N_p)/N_p - 0.33 I_x(-2/N_p)/N_p^2 \right\} dz'. \qquad (8)$$

In Eq. (8) N_p is a function of the propagation direction z'. In the limit of many pulses per flow time Eq. (8) approaches the cw result.
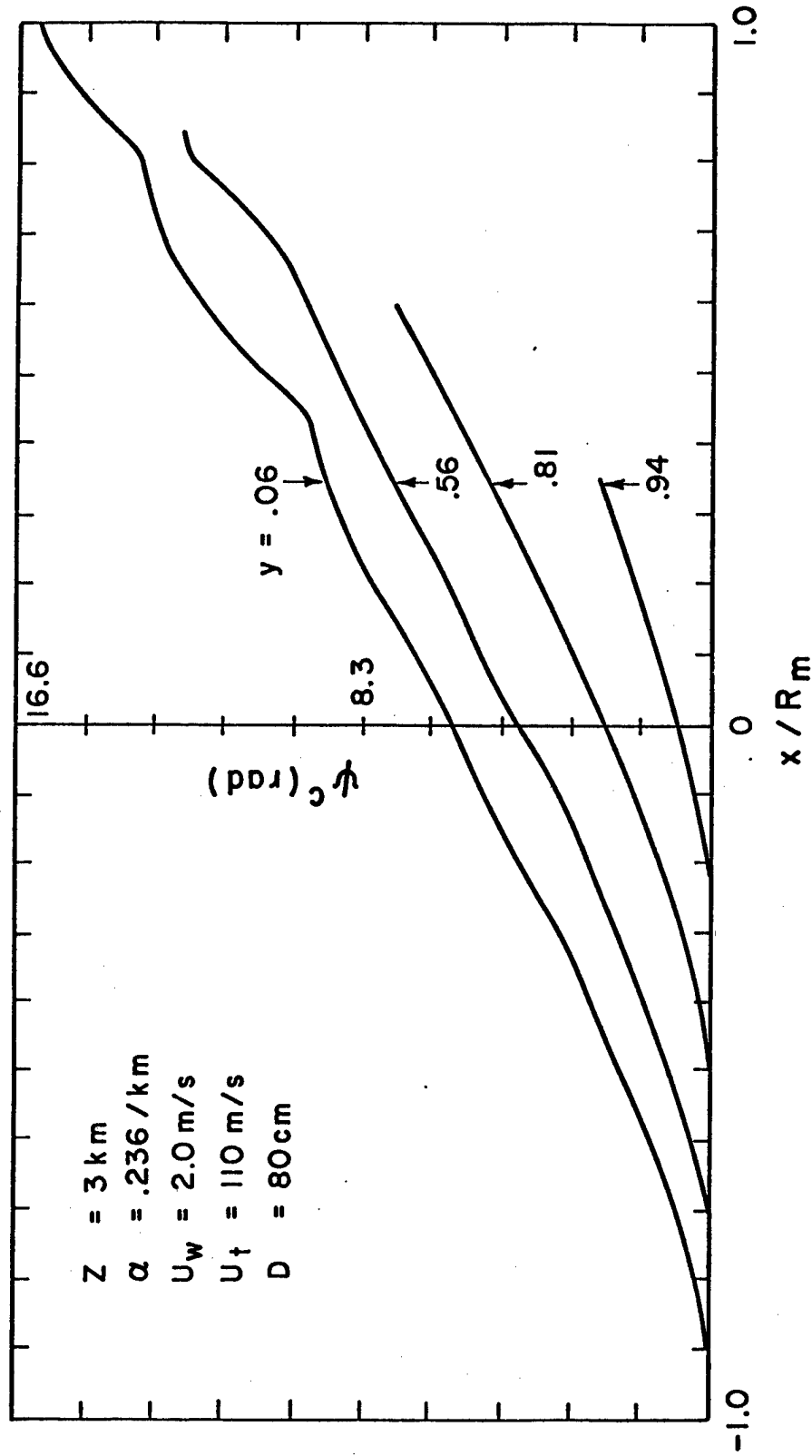
Fig. 1 Phase profiles for a beam focused at 3 km. The optical phase is expressed in radians and is shown at four different locations perpendicular to the beam motion. To obtain the non-dimensional distribution change the scale of ψ^c to unity. The propagation parameters are for standard atmospheric conditions.

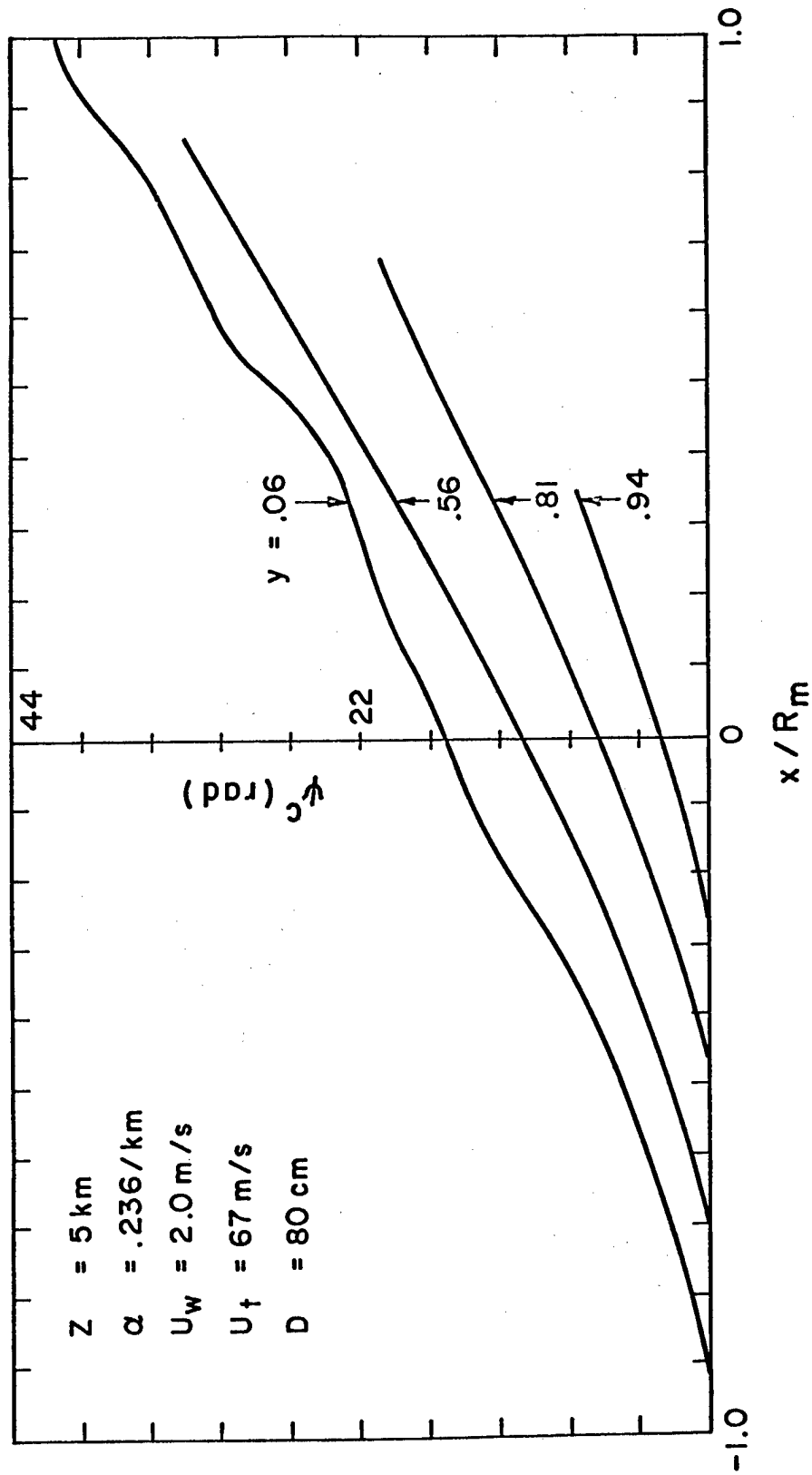# NORMALIZED PHASE PROFILES

Fig. 2 Phase profiles for a beam focused at 5 km. The transverse component of the target velocity is 67 m/s.

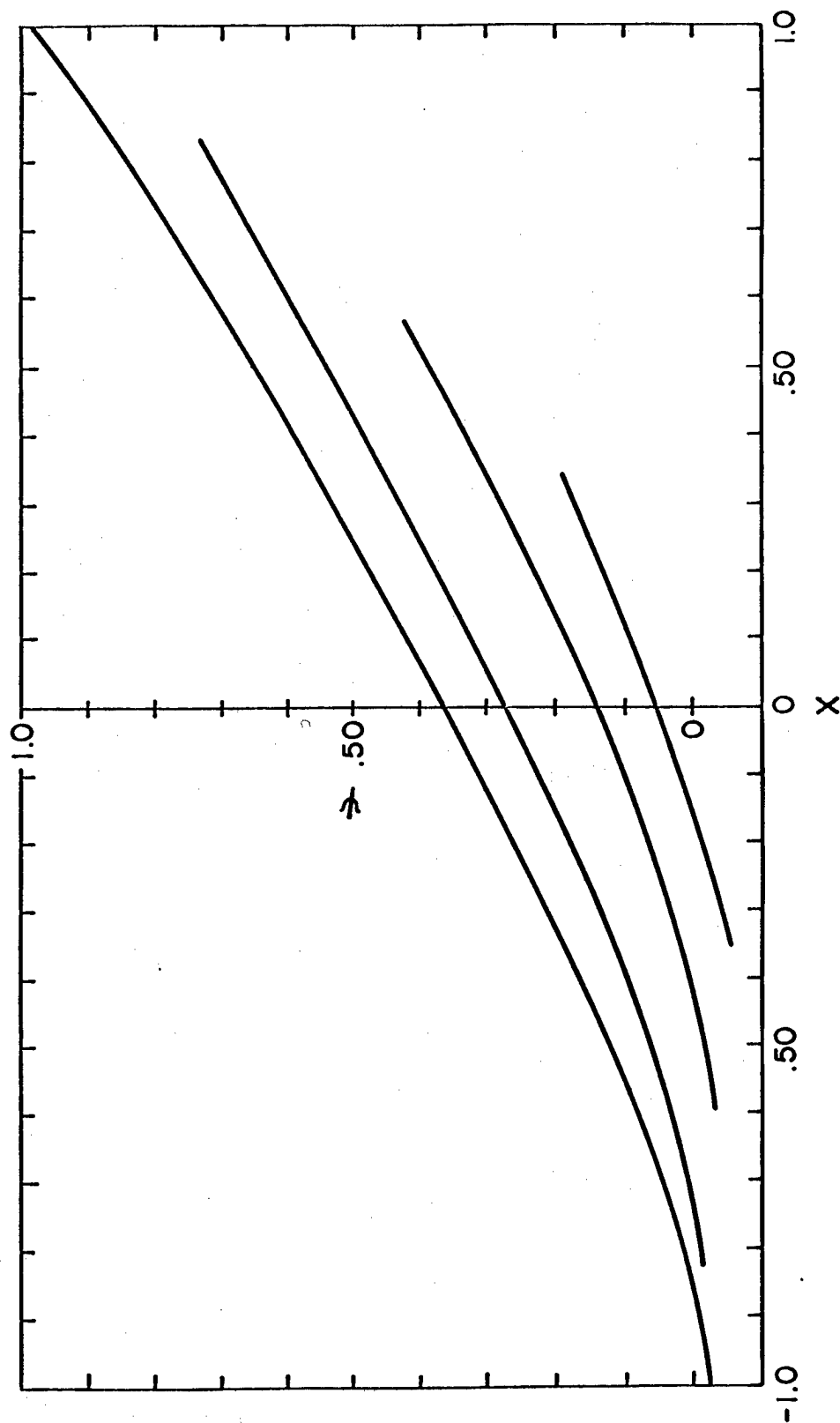ZERNIKE EXPANSION OF NORMALIZED PHASE

Fig. 3 Expansion of the normalized phase in Zernike polynomials. Comparison of the results with those in Fig. 1 indicates that Eq. (6) can be regarded as exact.

The major uncertainity in the analysis is the effect of the wind direction and this will now be discussed. Results for the mirror contours are presented in Fig. 4 for three different wind directions. The direction of the wind is indicated by the arrows and the wind speed is equal for all three cases. The beam is also slewed in the x-direction. The case $\theta_w = 0$ corresponds to that of Fig. 1. The mirror contours exhibit more sensitivity to the wind direction than the other variables such as absorption coefficient, wind speed and range. However by rotating the mirror contours for $\theta_w = 0$ we can generate the mirror contours for those cases where the wind direction varies between $-45°$ and $+45°$, measured from the slew direction. This is not true for wind directions greater than $45°$ as is evident for the $90°$ result. This completes the analysis for determining the mirror contours.
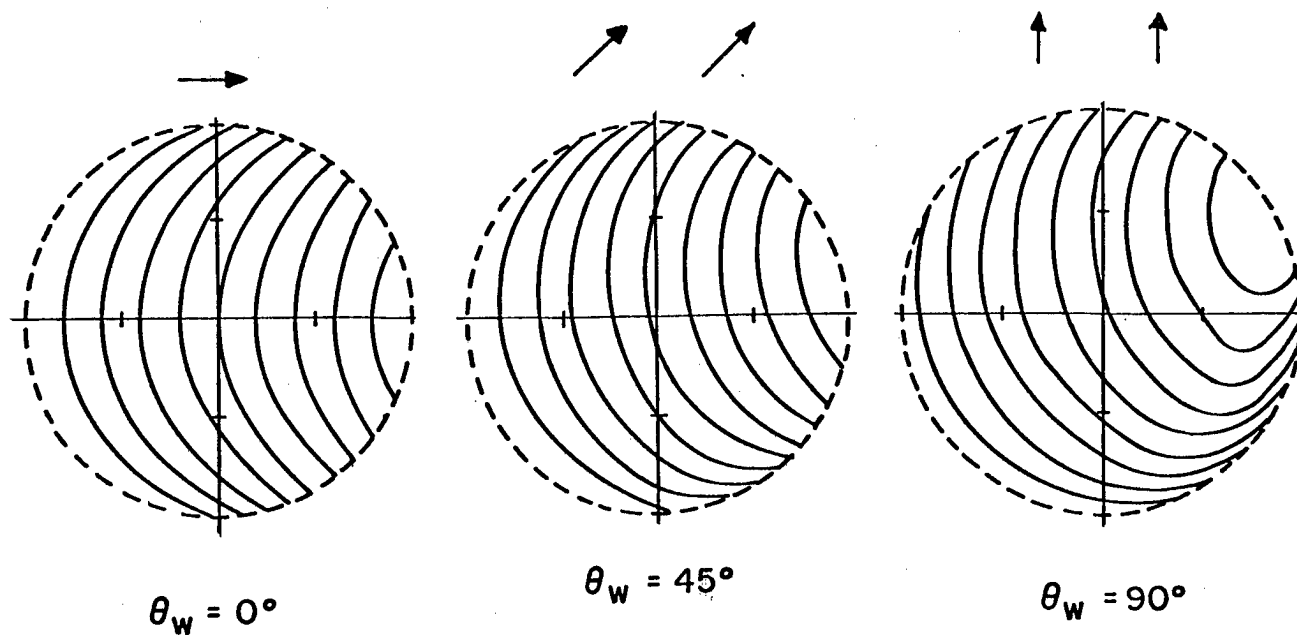
Fig. 4 Effects of wind direction on the mirror contours. Arrows indicate the direction of the wind. Beam is also slewed in x-direction. The contours for $\theta_w = 0$ correspond to those in Fig. 1.

III. IRRADIANCE AT THE FOCAL PLANE

We now present the results of a series of calculations for cases of interest to the Army. The laser is repetitively pulsed with a diameter of 80 cm, a uniform amplitude distribution, an energy per pulse of 10 KJ per pulse, and a focal point that varies between 3 and 5 kilometers. The absorption coefficient is 0.236 per km, the wind velocity is 2 m/s, and the transverse component of velocity at the target varies between 65 and 110 m/s.

In Fig. 5 we compare the irradiance distribution of the bloomed beam with the irradiance distributions for partial and complete compensation. For the bloomed beam the Strehl ratio is 0.25. With full compensation the Strehl ratio is 0.95, a factor of 4 increase in the irradiance. Essentially this gives a diffraction limited beam. Partial compensation involves correcting for the quadratic terms in Eq. (6) and results in a Strehl ratio of 0.80. Full compensation involves the fourth-order terms and requires more actuator elements. Partial compensation involves a defocusing in the direction of the beam motion and additional focusing in the perpendicular direction

The dependence, at 3 km, of the peak irradiance as a function of power is shown in Fig. 6. The bloomed irradiance also includes the effects of turbulence and jitter from the optical train. The strength of turbulence C_n^2 is 10^{-14} $m^{-2/3}$ and the jitter angle is 10 μr. For these conditions turbulence, at 10.6 μm, primarily causes beam wander rather than beam spreading. At 3 km removing the turbulent tilt and compensating for blooming gives a Strehl ratio of the order of 0.90. At P = 1MW the mirror contours are given in Fig. 1 and the irradiance distribution in Fig. 5. Fig. 7 presents the identical calculation

as that of Fig. 6 except that the range is increased from 3 km to 5 km and the transverse component of velocity at the focal plane reduced from 110 m/s to 62.5 m/s. The increase in range and decrease in velocity gives more severe blooming. Both beam wander and beam spreading by turbulence also occur. Removing the beam wander and correcting for blooming gives a factor of twenty increase in the irradiance. The Strehl ratio is of the order of 0.40. The phase contours associated with this calculation are given in Fig. 2.
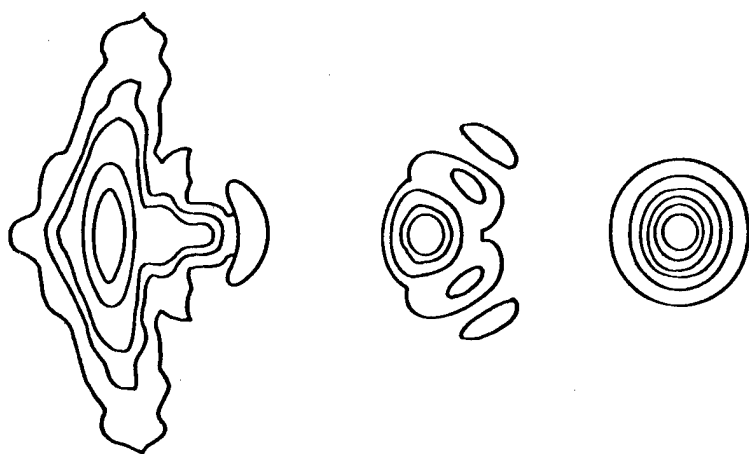
Fig. 5 Comparison of the irradiance distributions for a bloomed beam, a beam with compensation of the second order terms, and full blooming compensation. The atmospheric conditions are identical to those of Fig. 1.

COMPENSATED PEAK IRRADIANCES AT 3 km

$\lambda = 10.6 \mu m$ $U_W = 2 m/s$

$z = 3 km$ $U_t = 110 m/s$

$C_n^2 = 10^{-14} m^{-2/3}$
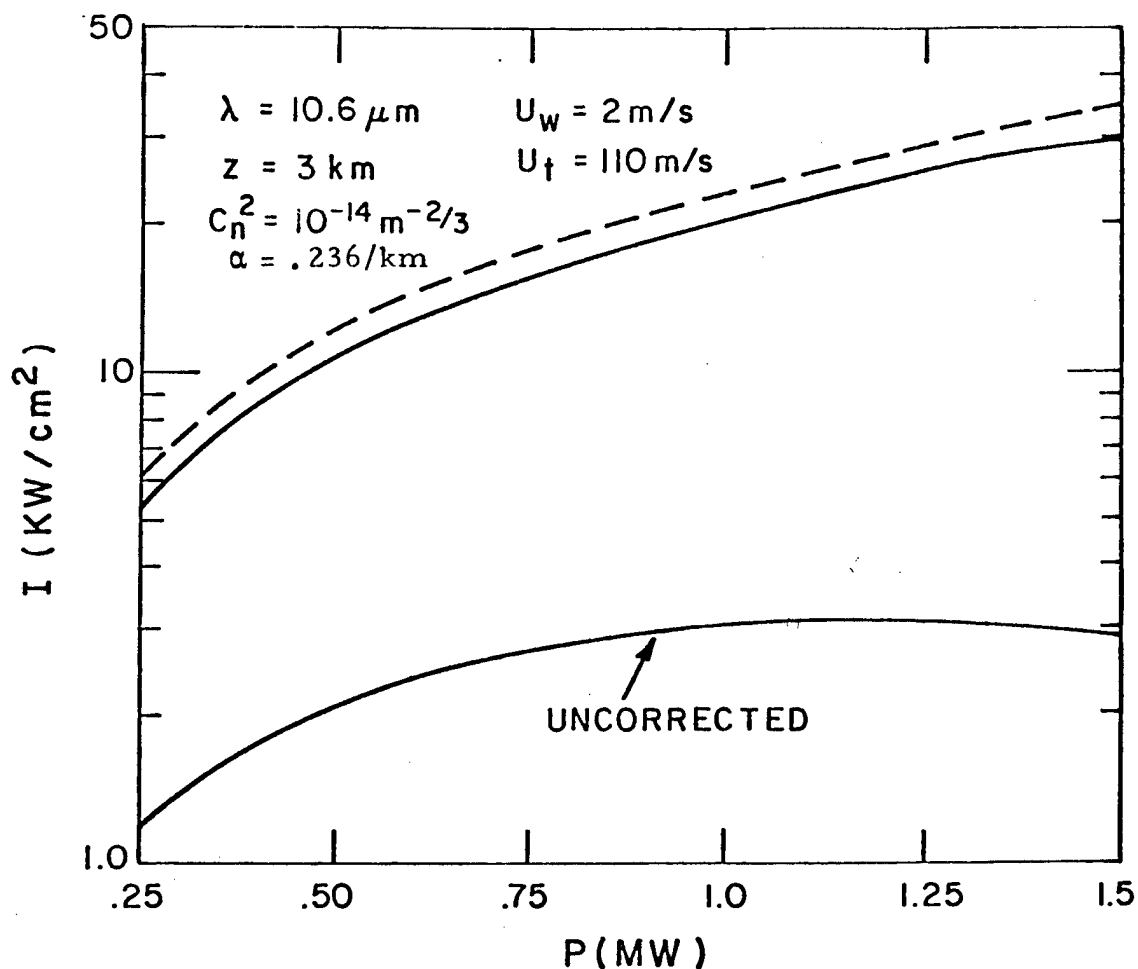
$\alpha = .236/km$

UNCORRECTED

I (KW/cm^2)

P(MW)

Fig. 6 Dependence of the peak irradiance at the focal plane for a 10.6 μm, repetitively pulsed laser. The beam has a diameter of 80 cm, a focal length of 3 km, a wind speed at the laser of 2m/s and a transverse component of the target velocity of 110m/s.
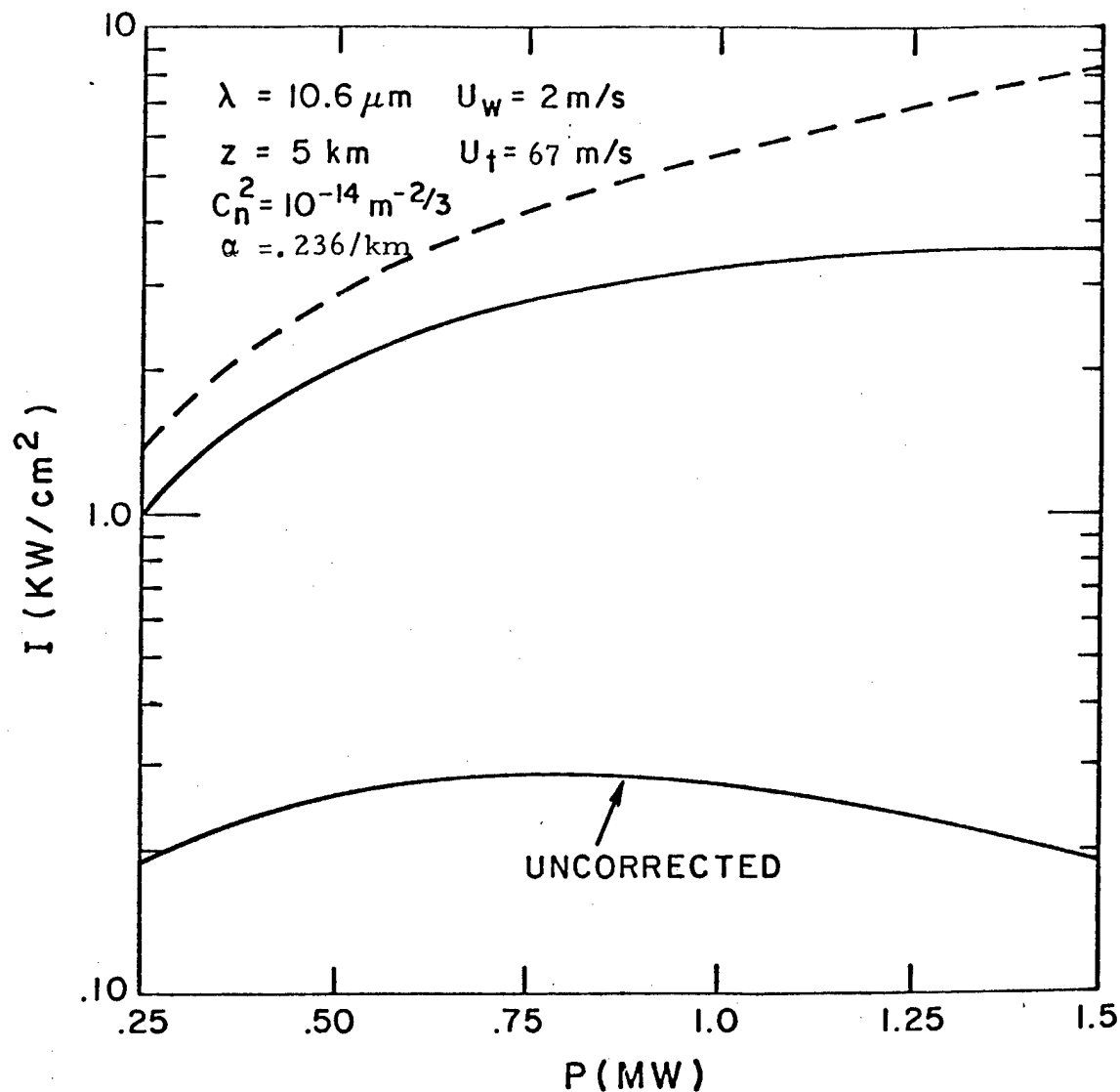
COMPENSATED PEAK IRRADIANCES AT 5 km

Fig. 7 Dependence of the peak irradiance at the focal plane for a 10.6 μm, repetitively pulsed laser. The beam has a diameter of 80 cm, a focal length of 5 km, a wind speed at the laser of 2m/s and a transverse component of the target velocity of 67m/s.

IV. CONCLUSIONS

Mirror contours that compensate for thermal blooming of a repetitively pulsed laser at 10.6 µm have been determined. These contours increase the irradiance at the focal plane up to a factor of ten. For Army applications of HEL systems the normalized mirror contours are insensitive to variations in the wind speed, absorption coefficient, range and altitude but are sensitive to the wind direction at the laser. An analytical expression for the mirror contours has also been presented. This expression is based upon an expansion in Zernike polynomials. The largest contributors are the tilt, refocus and astigmatic terms. Results for the irradiance distribution are compared for complete compensation and for compensation of the lowest order modes only. Including only the second order corrections significantly increases the irradiance. This requires fewer actuator elements to accomplish and, in practical situations, may be sufficient.

LIST OF REFERENCES

1. Whitney, Dr. Cynthia, <u>An Algebraic Model of Adaptive Optics for Continuous-Wave Thermal Blooming</u>, Charles Stark Draper Laboratory Report R-1235, January 1979.

2. Solodovnikov, V.V., <u>Introduction to the Statistical Dynamics of Automatic Control Systems</u>, translation edited by John B. Thomas and Lofti A. Zadeh, Dover Publications, Inc., New York.

3. Smith, D.C., "High-Power Laser Propagation: Thermal Blooming", <u>Proceedings of the IEEE</u>, December 1977.

4. Hogge, C.B., and R.R. Butts, "Frequency Spectra for the Geometric Representation of Wavefront Distortions Due to Atmospheric Turbulence", <u>IEEE Transactions on Antennas and Propagation</u>, March 1976.

5. <u>Adaptive Optics System Models In-Progress Technical Review</u>, The Analytic Sciences Corporation (TASC) Report SP-871-2, prepared for The Charles Stark Draper Laboratory, Inc., 17 May 1978.

6. Kaiser, Kenneth W., <u>Actuator Design Considerations for a Deformable Mirror</u>, Charles Stark Draper Laboratory Report C-5065, March 1978.

7. Kaiser, Kenneth W., <u>A Method for Improving the Performance of High-Energy Adaptive-Optics Deformable Mirrors</u>, Charles Stark Draper Laboratory Report C-4990, May 1978.

8. Wallace, James, <u>Theoretical Analysis of Adaptive Optics for Repetitively Pulsed Lasers</u>, Far Field, Inc., Sudbury, Massachusetts, prepared for CSDL under Purchase Order No. DL-H-162205, May 1979.

86